A Combinatorial Lipid Code Shapes the Electrostatic Landscape of Plant Endomembranes

Matthieu Pierre Platre, Lise Noack, Mehdi Doumane, Vincent Bayle, Mathilde Laetitia Audrey Simon, Lilly Maneta-Peyret, Laetitia Fouillen, Thomas Stanislas, Laia Armengot, Přemysl Pejchar, et al.

Article

Developmental Cell

A Combinatorial Lipid Code Shapes the Electrostatic Landscape of Plant Endomembranes

Highlights

- A charge gradient along the endocytic pathway defines an electrostatic territory
- PA accumulates to a significant level at the PM, in a DAG kinase-dependent manner
- The strong PM electrostatic field is powered by the additive effect of PI4P, PA, PS
- Curvature and PS/PI4P-driven electrostatics act as a dual TGN targeting signal

Authors

Matthieu Pierre Platre, Lise C. Noack, Mehdi Doumane, ..., Alenka Čopič, Patrick Moreau, Yvon Jaillais

Correspondence

yvon.jaillais@ens-lyon.fr

In Brief

Platre et al. show that plant plasma membrane-derived compartments each have a distinct electrostatic signature, set up by a combinatorial code of anionic phospholipids. This "electrostatic code" may represent a fundamental patterning principle of the endomembrane system and be a key determinant in protein targeting.

Platre et al., 2018, Developmental Cell *45*, 465–480
May 21, 2018
https://doi.org/10.1016/j.devcel.2018.04.011

CellPress

Developmental Cell
Article

A Combinatorial Lipid Code Shapes the Electrostatic Landscape of Plant Endomembranes

Matthieu Pierre Platre,[1] Lise C. Noack,[1] Mehdi Doumane,[1] Vincent Bayle,[1] Mathilde Laetitia Audrey Simon,[1] Lilly Maneta-Peyret,[2] Laetitia Fouillen,[2,3] Thomas Stanislas,[1] Laia Armengot,[1] Přemysl Pejchar,[4] Marie-Cécile Caillaud,[1] Martin Potocký,[4] Alenka Čopič,[5] Patrick Moreau,[2,6] and Yvon Jaillais[1,7,*]

[1]Laboratoire Reproduction et Développement des Plantes, Université de Lyon, ENS de Lyon, UCB Lyon 1, CNRS, INRA, Lyon 69342, France
[2]UMR 5200 Membrane Biogenesis Laboratory, CNRS-University of Bordeaux, Bâtiment A3 - INRA Bordeaux Aquitaine, 71 Avenue Edouard Bourlaux- CS 20032, Villenave d'Ornon 33140, France
[3]Metabolome-Lipidome Facility of Bordeaux, Functional Genomics Center, Villenave d'Ornon, France
[4]Institute of Experimental Botany, Czech Academy of Sciences, 16502 Prague 6 - Lysolaje, Czech Republic
[5]Institut Jacques Monod, CNRS, UMR 7592, Université Paris Diderot, Sorbonne Paris Cité, Paris 75013, France
[6]Bordeaux Imaging Center, UMS 3420 CNRS, US4 INSERM, University of Bordeaux, Bordeaux 33000, France
[7]Lead Contact
*Correspondence: yvon.jaillais@ens-lyon.fr
https://doi.org/10.1016/j.devcel.2018.04.011

SUMMARY

Membrane surface charge is critical for the transient, yet specific recruitment of proteins with polybasic regions to certain organelles. In eukaryotes, the plasma membrane (PM) is the most electronegative compartment of the cell, which specifies its identity. As such, membrane electrostatics is a central parameter in signaling, intracellular trafficking, and polarity. Here, we explore which are the lipids that control membrane electrostatics using plants as a model. We show that phosphatidylinositol-4-phosphate (PI4P), phosphatidic acidic (PA), and phosphatidylserine (PS) are separately required to generate the electrostatic signature of the plant PM. In addition, we reveal the existence of an electrostatic territory that is organized as a gradient along the endocytic pathway and is controlled by PS/PI4P combination. Altogether, we propose that combinatorial lipid composition of the cytosolic leaflet of organelles not only defines the electrostatic territory but also distinguishes different functional compartments within this territory by specifying their varying surface charges.

INTRODUCTION

An evolutionarily conserved feature of cellular organelles is the distinct phospholipid composition of their membranes, which is essential to specify their identity and function. Within the endomembrane system of animal cells, the existence of two major lipid territories has been postulated, one characterized by membranes with loose lipid packing, and the other defined by membrane surface charges (Bigay and Antonny, 2012). These two lipid territories correspond roughly to two dynamic membrane-recycling systems; one centered on the ER and that includes membranes from the ER, the nuclear envelope, and the *cis*-Golgi, and the other centered on the plasma membrane (PM) and that comprises the *trans*-Golgi, the *trans*-Golgi network (TGN), the PM and endosomes (Bigay and Antonny, 2012). In the latter, referred to as the electrostatic territory, negative charges carried by anionic phospholipids recruit proteins with polybasic regions and as such participate in the localization of a large number of cellular factors along the endocytic pathway (Bigay and Antonny, 2012). A second characteristic of the electrostatic territory lays in the finding that it is not uniformly organized across all PM-derived organelles (Bigay and Antonny, 2012; Yeung et al., 2006). Rather, the inner leaflet of the PM is the most electronegative cytosolic-facing membrane across eukaryotes, including yeasts, animals, and plants (Moravcevic et al., 2010; Simon et al., 2016; Yeung et al., 2006). This PM electrostatic signature is critical for cell signaling, as it enables to specifically recruit proteins to the PM, such as, e.g., small GTPases, kinases, or kinase regulators (Noack and Jaillais, 2017).

Anionic phospholipids are minor lipids in membranes and include phosphatidylinositol phosphate (also known as phosphoinositides, PIPs), as well as phosphatidic acid (PA) and phosphatidylserine (PS). The respective importance of these lipids in powering the membrane electrostatic field is not strictly proportional to the respective amount of this lipid in a given membrane. Indeed, cellular membranes are highly asymmetric and have very different lipid composition in their cytosolic and luminal/outer leaflets (Bigay and Antonny, 2012). This is notably relevant for PS, which is produced in the luminal leaflet of the ER and has to be flipped into the cytosolic leaflet to contribute to membrane electrostatics (Fairn et al., 2011; Xu et al., 2013). In addition, different anionic lipids have different net negative charges. In particular, phosphoinositides are polyanionic lipids and have a larger impact on the local electrostatic field as compared to PA and PS (Li et al., 2014). Furthermore, anionic phospholipids have different pKa values and their negative charges may vary depending on their local environment. Finally, at any given time, many anionic lipids are in complex with endogenous

proteins in cells. Since ionic protein-lipid interactions directly involve the negative charge of anionic lipid head groups, these interactions mitigate the net contribution from these lipids to the electrostatic field. As such, the lipids that are important to power membrane electrostatics *in vivo* may not be simply the most abundant anionic lipids, and cannot be determined by direct biochemical measurement of lipid accumulation. To bypass this complexity, we opted to use an *in planta* biosensor approach. Indeed, lipid sensors preferentially reveal the pool of lipids that are facing the cytosol and available for the probes, while lipids that are tightly bound to endogenous proteins will be masked.

We recently established that PI4P is the main phosphoinositide required to power the high electrostatic field of the plant PM, while $PI(4,5)P_2$ is dispensable for PM surface charges (Simon et al., 2016). Here, we addressed whether an electrostatic territory exists beyond the PM in plant cells. To do so, we studied the contribution of PA and PS to membrane surface charge and how they may cooperate with PI4P to establish the electrostatic territory. We demonstrate that PA and PS act in concert with PI4P to generate the distinctively high PM electrostatic field. In addition, we reveal the existence of an electrostatic gradient along the endocytic pathway, which is highest at the PM, intermediate in early endosomes/*trans*-Golgi network (EE/TGN), and lowest in late endosomes (LE). We further show that PS, in combination with PI4P, organizes this intracellular electrostatic gradient. Finally, we find that the coincident detection of membrane curvature and electrostatics provides a signal for EE/TGN targeting. To conclude, each PM-derived organelle has a distinct electrostatic signature that is set up by a combinatorial code of various anionic phospholipids. We propose that this "electrostatic code" may represent a fundamental patterning principle of the endomembrane system and acts as a key determinant of protein subcellular targeting.

RESULTS

PA Sensors Accumulate at the PM Cytosolic Leaflet in *Arabidopsis* Root Epidermis

PA is an anionic phospholipid, which accumulates in the subapical region of the PM cytosolic leaflet in tobacco pollen tubes (Potocky et al., 2014). To analyze whether PA could also localize at the PM in *Arabidopsis* sporophytic tissues, and thereby may contribute to PM electrostatics, we raised transgenic *Arabidopsis* lines stably expressing mCITRINE (mCIT)-tagged variants of the recently developed "*PA biosensor with superior sensitivity*" (mCIT-1xPASS and mCIT-2xPASS) (Zhang et al., 2014) under the control of the ubiquitous promoter of the *UBIQUITIN10* (*UBQ10*) gene. This PA probe is based on the PA-binding motif of the yeast Spo20p protein, with an extra nuclear export signal (NES) to exclude the fusion protein from the nucleus and increase the accessibility of the probe to the cytoplasm (Zhang et al., 2014). Both mCIT-1xPASS and mCIT-2xPASS sensors were targeted to the PM in *Arabidopsis*, including root and shoot tissues (Figure 1A, Figures S1A and S1B). We noticed that these PA probes localized early at the cell plate (Video S1), where it colocalized with the endocytic dye FM4-64 (Figure S1C). Furthermore, mCIT-2xPASS localized on the flank region of growing root hairs (Video S2), in a pattern resembling the localization of PA sensors in growing tobacco pollen tubes (Potocky et al., 2014). While both PA sensors localized at the PM, mCIT-1xPASS was also cytosolic, while mCIT-2xPASS accumulated in the nucleus (Figure 1A). This suggests that in mCIT-2xPASS, the NES is not as efficient as in the mCIT-1xPASS probe. Consistently, the mCIT-1xPASS probe for which the NES is mutated ($1xPASS^{NESmut}$) localized at the PM, the cytosol, and in the nucleus (Figure 1A). It is unclear what the significance of the nuclear localization of the probe is. Indeed, it might reflect uncontrolled diffusion from the cytosol into the nucleus or trapping of the probe in the nucleus by nuclear PA. Of note, for all three transgenic lines (mCIT-1xPASS, $mCIT\text{-}1xPASS^{NESmut}$, mCIT-2xPASS), we observed some variability in the intensity of PM labeling between different roots. Although the cause of this variability is currently unknown, it might arise from different stress status of individual roots or cells since PA metabolism is well known to be under tight environmental control (Testerink and Munnik, 2011). Accordingly, cold treatment, which is known to trigger PA synthesis (Testerink and Munnik, 2011), promoted the localization of mCIT-1xPASS at the PM (Figure S1E). Nonetheless, the three aforementioned probes are targeted to the PM of root meristematic cells (Figure 1A), suggesting local enrichment of PA in this membrane even in normal growing conditions (i.e., non-stressed).

In order to validate the PA sensor specificity *in planta*, we first expressed mCIT-1xPASS mutant versions (L67P single mutant, K66E-K68E double mutants [2K > E] and K66E-K68E-K71E-K73E quadruple mutants [4K > E]), which were previously shown to impair PA binding (Potocky et al., 2014; Zhang et al., 2014). $mCIT\text{-}1xPASS^{2K>E}$ retained a faint PM labeling, while $mCIT\text{-}1xPASS^{L67P}$ and $mCIT\text{-}1xPASS^{4K>E}$ were fully soluble, suggesting that lipid binding is required for the PM localization of the 1xPASS probe (Figure 1A). Diacylglycerol kinases (DGK) are the major PA-producing enzymes at the PM of animal cells with constitutively elevated PA level (Bohdanowicz et al., 2013). To test the importance of DGKs in producing PA at the PM of unstressed plants, we used R59949 and R59022, two inhibitors of DGK activity. R59022 was previously validated as an inhibitor of plant DGKs both *in vitro* and *in vivo* (Gomez-Merino et al., 2005; Ruelland et al., 2002). In addition, we found that both DGK inhibitors reduced bulk PA levels by about 50%–60%, while having minor effects on bulk PC, PI, and PS content (Figure 1B). Both inhibitors induced the release of mCIT-1xPASS and mCIT-2xPASS PA probes from the PM into the cytosol and nucleus, respectively (Figures 1C and S1D). To confirm that the dissociation of mCIT-1xPASS was caused by inhibition of PA production in R59949-treated seedlings, we performed add-back experiments by supplementing the root with exogenous lysophosphatidic acid (lyso-PA) or lysophosphatidylserine (lyso-PS) as control. We used lysophospholipids since they have identical head groups as PA/PS but are more soluble than phospholipids and as such are more likely to reach the cytosolic leaflet of cellular membranes (Maeda et al., 2013; Moser von Filseck et al., 2015). We found that upon inhibition of endogenous PA production by R59949, mCIT-1xPASS was maintained at the PM in presence of an exogenous supply of lyso-PA but not in the presence of lyso-PS (Figure 1E). Moreover, in the presence of either R59949 or R59022, reporters for PI4P, $PI(4,5)P_2$, and PS anionic phospholipids ($mCIT\text{-}1xPH^{FAPP1}$, $mCIT\text{-}1xPH^{PLC}$, and $mCIT\text{-}C2^{Lact}$, respectively [Simon et al.,

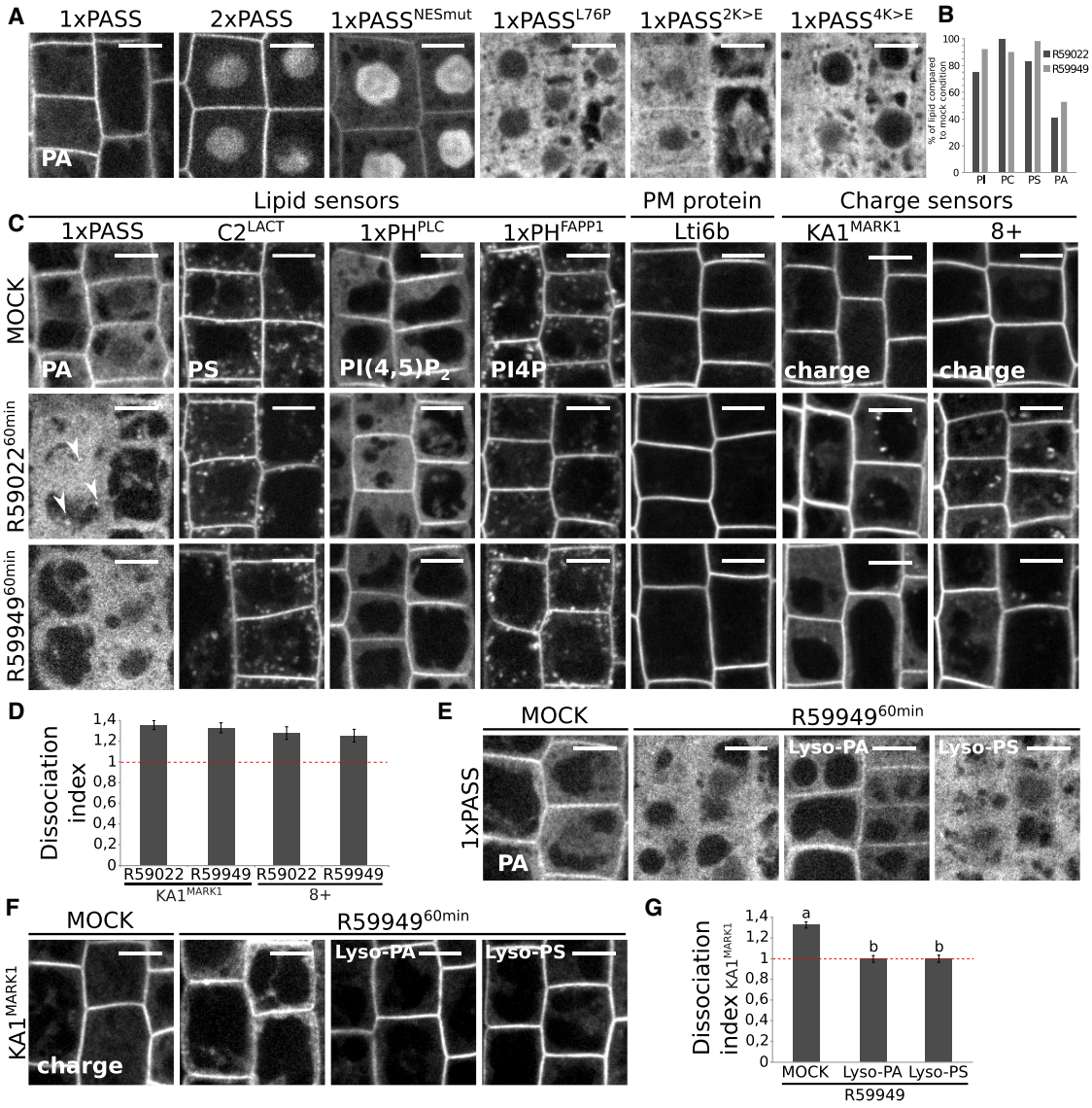

Figure 1. DAG Kinase-Dependent Accumulation of Phosphatidic Acid at the PM Is Required to Maintain the Electrostatic Field of the PM Cytosolic Leaflet

(A) Confocal images of *Arabidopsis* root epidermis expressing mCIT-tagged PA reporters.

(B) Quantification of bulk phosphatidylcholine (PC), phosphatidylinositol (PI), PS, and PA in mock, R59022, and R59949 (12.5 μM, 60 min) treated seedlings. Results are expressed as the ratio of each lipid species in the mock and treated condition.

(C) Confocal images of plants expressing mCIT/GFP-tagged reporters in mock conditions, 12.5 μM R59022 or 12.5 μM R59949 for 60 min. Arrows highlight the presence of spots.

(D) Quantification of the mCIT-KA1^{MARK1} and mCIT$^{8K-Farn}$ (8+) dissociation index (mean ± SEM), upon R59022 and R59949 treatment (n = 150 cells 12.5μM, 60 min).

(E–G) Confocal images of *Arabidopsis* root epidermis expressing mCIT-1xPASS (E) or mCIT-KA1^{MARK1} (F) upon concomitant lyso-PA or lyso-PS and R59949 (12.5 μM) treatment (60 min) and (G) quantification of related mCIT-KA1^{MARK1} dissociation index (mean ± SEM) (n = 150). Different letters indicate significant differences among means (p value = 0.05, Kruskal-Wallis bilateral test). Scale bars, 5 μm.

See also Figure S1, Videos S1 and S2.

2014, 2016]), were still localized at the PM (Figure 1C). In addition, both R59949 and R59022 treatments had no impact on the localization of EGFP-Lti6b (Figure 1C), a control protein with two transmembrane segments and very short cytosolic tails, whose localization is not regulated by anionic lipids (Cutler et al., 2000). Altogether, these results indicate that the PM localization of the mCIT-1xPASS and mCIT-2xPASS probes are largely driven by DGK-synthesized PA, and suggest that PA accumulates in the cytosolic leaflet of the plant PM.

PA Contributes to PM Cytosolic Leaflet Surface Charges

We next asked whether PA could participate in the electrostatic property of the PM. We took advantage of DGK inhibitors to reduce the level of PA at the PM and analyzed the impact of

this pharmacological inhibition on the localization of membrane surface charge reporters. We used two types of membrane charge reporters that we previously validated *in planta* (Simon et al., 2016). The first probe, mCIT$^{8K-Farn}$ corresponds to two mCITRINE fluorescent proteins fused in tandem, which localize in electrostatic membranes thanks to the combinatorial effects of a polycationic region (with eight net positive charges, +8) and an adjacent farnesyl lipid anchor, which provides hydrophobic anchoring (Simon et al., 2016; Yeung et al., 2006). The second probe corresponds to the KA1 domain of the human protein MARK1, which is a folded unit known to interact non-stereospecifically with all anionic phospholipids (Moravcevic et al., 2010). We found that in PA-depleted condition, charge sensors (mCIT$^{8K-Farn}$ and mCIT-KA1^{MARK1} probes) were released into the cytosol and endosomes (Figures 1C and 1D). Endosome labeling was more prominent with R59022 than R59949 treatment and correlated with the concomitant accumulation of mCIT-1xPASS in similar compartments (see arrows, Figure 1C). To test whether the loss of the PM localization of our membrane surface charge markers was primarily due to loss of negative charges carried by the PA head group or by modifications of other membrane properties due to the lack of PA, we conducted lyso-PA and lyso-PS add-back experiments. Consistent with the finding that lyso-PA add-back was able to rescue the localization of the mCIT-1xPASS PA sensor in R59949-treated seedlings (Figure 1E), this treatment also complemented the PM localization of mCIT-KA1^{MARK1} charge sensor (Figures 1F and 1G). However, in contrast to mCIT-1xPASS, whose localization upon R59949 treatment was not rescued by lyso-PS add-back (Figure 1E), the localization of mCIT-KA1^{MARK1} was complemented by this treatment (Figures 1F and 1G). This experiment showed that addition of negative charges via lyso-PS treatment was able to substitute the negative charges normally carried by PA. Therefore, the loss of charges induced by PA depletion rather than changes in other membrane properties is likely causal to the loss of PM electrostatics induced by the R59949 treatment. Together, our results suggest that PA contributes to the electrostatic properties of the plasmalemma cytosolic leaflet.

PS Sensors Accumulate on the Cytosolic Leaflet of PM and PM-Derived Organelles

To evaluate the potential function of PS in membrane electrostatics, we studied its subcellular distribution using genetically encoded biosensors that report the localization of PS in inner membrane leaflets. We used the stereospecific PS-binding C2 domain of bovine Lactadherin (C2^{LACT}) and the pleckstrin homology (PH) domain of human EVECTIN2 (PH^{EVCT2}). These probes were extensively validated as calcium-independent PS reporters (Chung et al., 2015; Moravcevic et al., 2010; Moser von Filseck et al., 2015; Uchida et al., 2011; Yeung et al., 2008) (Figures S2A and S2B). We raised transgenic *Arabidopsis* plants that stably express fluorescent fusions with either C2^{LACT}, or 2xPH^{EVCT2} under the control of the *UBQ10* promoter. As we previously reported for mCIT-C2^{LACT} in root epidermis (Simon et al., 2016), we found that the C2^{LACT} domain was localized at the PM and in multiple intracellular compartments in all cell types analyzed, including both shoot and root tissues (Figures 2A and S2C–S2J). We noticed that in tip-growing cells, such as root hairs and pollen tubes, C2^{LACT} was localized to the shank region of the PM and intracellular compartments and accumulated in the inverted cone region at their very tip (Videos S3 and S4, respectively), a region known for active endocytic and exocytic activities (Noack and Jaillais, 2017). In addition, the mCIT-2xPH^{EVCT2} reporter showed a similar localization pattern as mCIT-C2^{LACT} and, consistently, tdTOMATO-2xPH^{EVCT2} extensively colocalized with mCIT-C2^{LACT} (Figure S2C). However, similarly to animal cells (Chung et al., 2015; Uchida et al., 2011; Yeung et al., 2008), we noticed that mCIT-C2^{LACT} PM localization was more pronounced than that of mCIT-2xPH^{EVCT2}/tdTOMATO-2xPH^{EVCT2} (Figure S2C).

Next, we analyzed in which endomembrane structures the C2^{LACT} probe localized. We crossed the mCIT-C2^{LACT} reporter line with various red-fluorescent membrane marker lines or imaged it in conjunction with red-fluorescent dyes (Figure 2A). mCIT-C2^{LACT} colocalized with the plasmalemmal marker Lti6b-2xmCHERRY (mCh) (Elsayad et al., 2016), confirming that this PS sensor accumulates at the PM (Figure 2A). We also found that mCIT-C2^{LACT} was localized along the endocytic pathway, as it colocalized with the endocytic tracer FM4-64 and its localization was sensitive to both the fungal toxin brefeldin A (BFA) and wortmannin (Wm, Figure 2A), two drugs that affect the morphology of early and late endocytic compartments, respectively (Bayle et al., 2017; Geldner et al., 2009). Finally, we observed in few meristematic cells (14.3% SEM ± 2.73, n = 458 cells) that mCIT-C2^{LACT} colocalized with the tonoplast marker VHA-A3-mRFP1 (Figure 2A) (Dettmer et al., 2006). We also found that mCIT-C2^{LACT} localized on forming cell plate during cytokinesis, together with FM4-64 and PI4P (Figure S2K and Video S5). Therefore, PS accumulation at the cell plate together with PA and PI4P correlates with the acquisition of the cell plate electrostatic identity (Simon et al., 2016). Together, our results suggest that PS accumulates at the PM and cell plate, as well as in PM-derived organelles.

PS Is Sufficient to Maintain Negative Surface Charges on the PM Cytosolic Leaflet

Next, we addressed whether PS contributes to PM electrostatics. Because there is no chemical compound known to directly inhibit PS production, we tested whether PS could be involved in PM electrostatics by depleting all other anionic phospholipids from this membrane through chemical inhibition. We previously validated the use of PAO, a PI4-Kinase inhibitor, to interfere with PM phosphoinositides production (Simon et al., 2016). We showed that short-term treatment (15–30 min) significantly depleted PI4P but not PI(4,5)P_2 pools, while longer treatment (>60 min) affected the synthesis of both lipids (Simon et al., 2016). In order to concomitantly deplete the plant PM from PA, PI4P and PI(4,5)P_2, leaving PS as the sole anionic lipid in this membrane, we used a combination of R59949 or R59022 (60 min, as described in Figure 1) and prolonged PAO treatment (120 min). This treatment efficiently displaced PI4P, PI(4,5)P_2, and PA sensors from the PM to the cytosol, while the PM localization of EGFP-Lti6b and mCIT-C2^{LACT} were largely unaffected by this treatment (Figure 2B). As expected, a proportion of mCIT$^{8K-Farn}$ and mCIT-KA1^{MARK1} charge reporters were found in the cytosol in this condition (Figure 2B). However, both charge reporters retained a degree of PM localization that can be attributed to PS, the only remaining anionic lipid in this membrane.

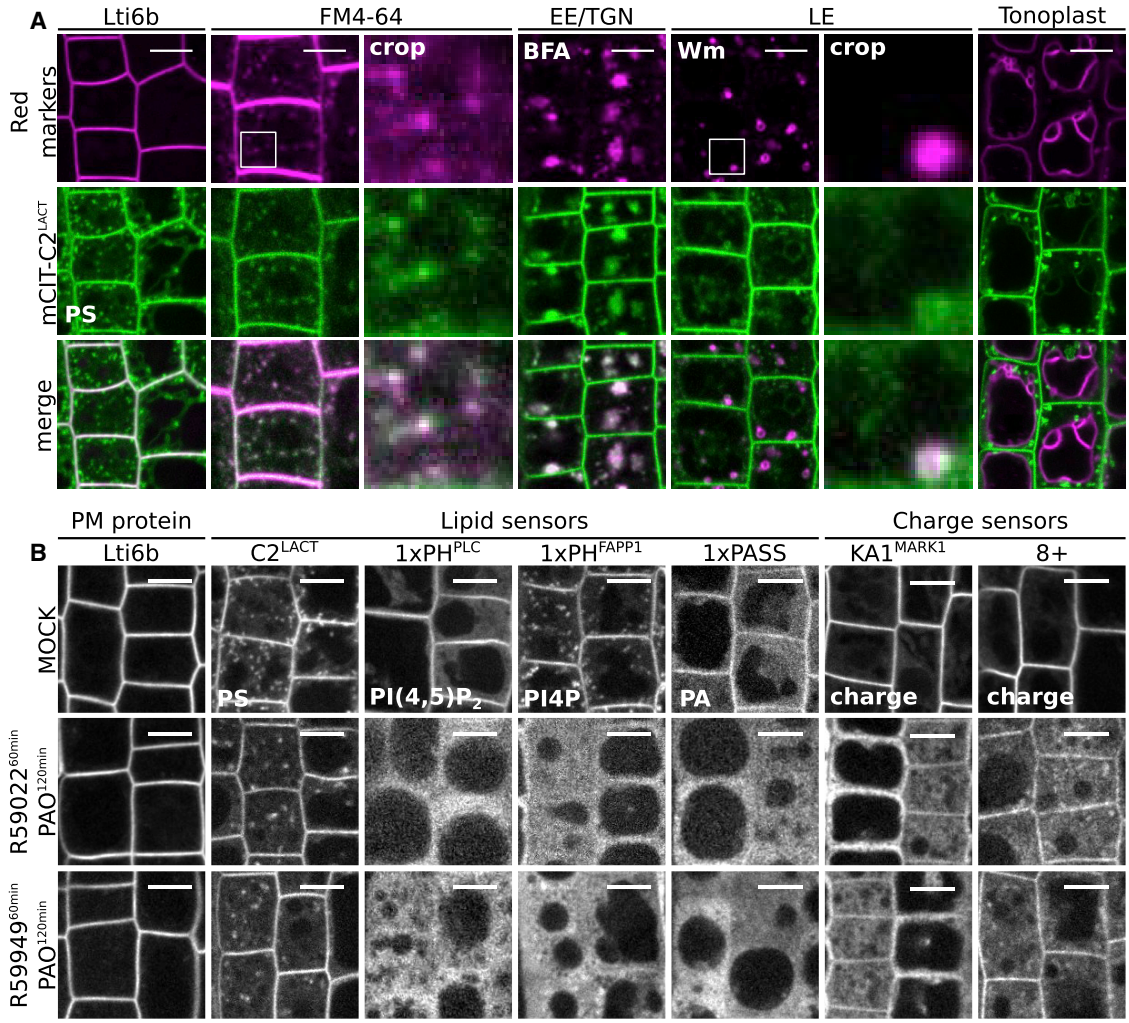

Figure 2. Phosphatidylserine Accumulates at the PM and along the Endocytic Pathway and Is Sufficient to Maintain Negative Charges at the PM Cytosolic Leaflet

(A) Confocal images of *Arabidopsis* root epidermis co-expressing a red fluorescence marker (magenta), mCIT-C2^{LACT} (PS, green), and corresponding merge. Top images: Lti6b-2xmCH (PM marker), FM4-64 (endocytic tracer, 1 μM, 60 min), VHA-A1-mRFP (EE/TGN marker) in the presence of brefeldin A (BFA, 25 μM, 60 min), W7R (LE marker) treated with 30 μM wortmannin (Wm, 30 μM, 90 min), VHA-A3-mRFP (tonoplast marker).

(B) Confocal images of plants expressing mCIT/GFP-tagged reporters in mock conditions, plants pre-treated with 30 μM PAO for 60 min and then 12.5 μM R59022 and 30 μM PAO for 60 min, plants pre-treated with 30 μM PAO for 60 min and then 12.5 μM R59949 and 30 μM PAO for 60 min. Scale bars, 5 μm. See also Figure S2, Videos S3, S4, and S5.

Therefore, in this condition, PS appears to be sufficient to maintain a certain degree of surface charges at the PM.

Phosphatidylserine Synthase1 Mutants Do Not Produce Any PS but Are Viable

In order to analyze the impact of PS depletion on membrane surface charges, we characterized mutants in the *PHOSPHATIDYLSERINE SYNTHASE1* (*PSS1*) gene (Yamaoka et al., 2011). We isolated three *pss1* alleles that we named *pss1-3*, *pss1-4*, and *pss1-5* (Figure 3A). These three alleles expressed no detectable full-length *PSS1* cDNA (Figure S3A), and segregated as single recessive mutants without any distorted segregation (Figure S3B). All three alleles showed the same sporophytic phenotype, the *pss1* mutants being severely dwarfed both at the shoot and root levels (Figures 3B and S3F–S3I). In addition, these mutants were sterile and had to be propagated as heterozygous. Introduction of a wild-type copy of the *PSS1* gene fully complemented the *pss1-3* shoot phenotype (Figures 3B, S3D, and S3F). High-performance thin-layer chromatography (HPTLC) and liquid chromatography-tandem mass spectrometry (LC-MS/MS) lipidomic analyses showed that *pss1-3* and *pss1-4* did not produce any PS (Figures 3C and 3D and Table S1). Importantly, these analyses suggested that both alleles led to only minor changes in their overall phospholipid content (Figures 3C and S3C). To confirm these biochemical analyses, we introgressed mCIT-C2^{LACT} and mCIT-2xPH^{EVCT2} into the *pss1-3* mutant. In contrast to the wild-type situation, we could detect only a faint signal for mCIT-C2^{LACT} in *pss1-3*, suggesting that in the absence of PS, mCIT-C2^{LACT} is unstable in plant cells (Figure 3E). Consistently, exogenously treating mCIT-C2^{LACT}/*pss1-3*

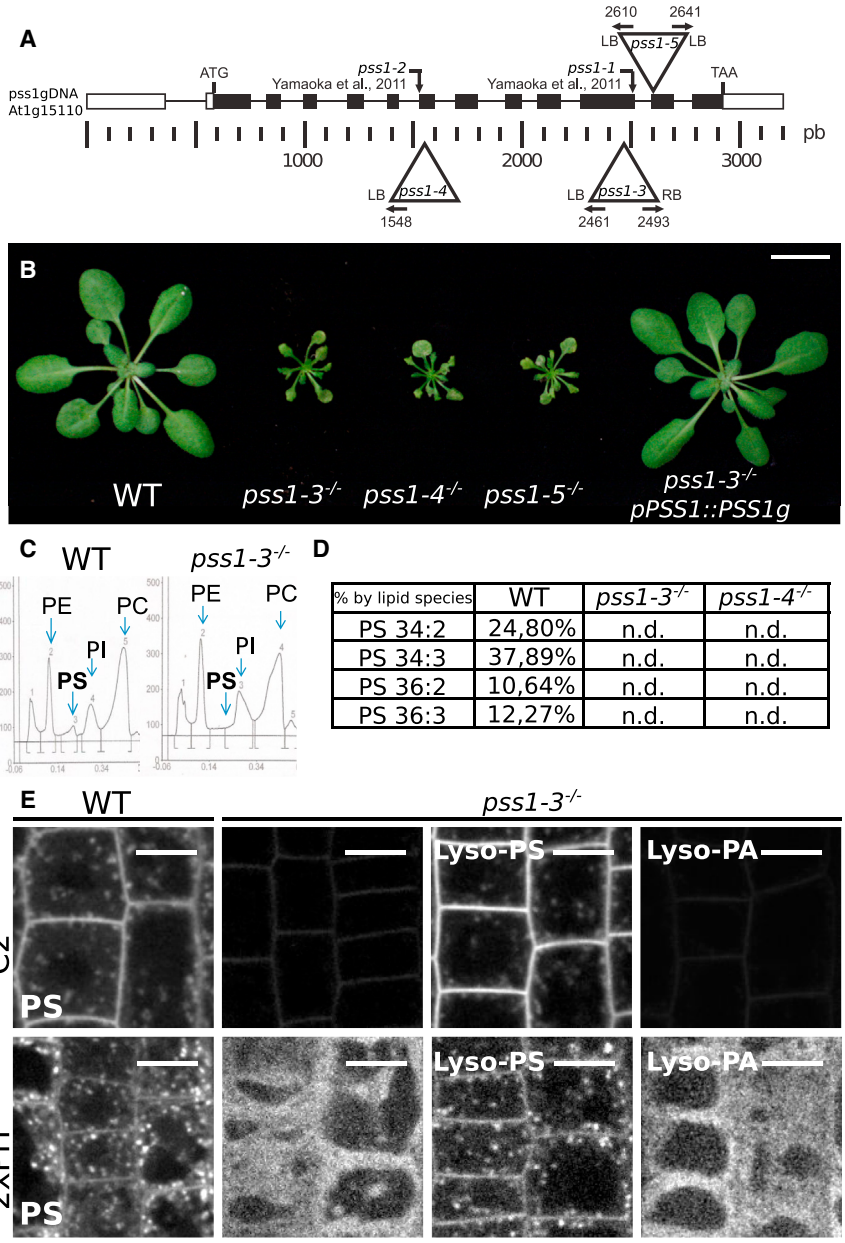

% by lipid species	WT	*pss1-3*$^{-/-}$	*pss1-4*$^{-/-}$
PS 34:2	24,80%	n.d.	n.d.
PS 34:3	37,89%	n.d.	n.d.
PS 36:2	10,64%	n.d.	n.d.
PS 36:3	12,27%	n.d.	n.d.

Figure 3. *PSS1* Is Required for PS Biosynthesis and Plant Growth

(A) Schematic representation of transfer DNA insertions in *PSS1*. LB, left border; RB, right border; numbers indicate the position of border/*PSS1* junctions.

(B) Rosette phenotype of *pss1* mutants compared with the wild-type (WT). Scale bar, 2 cm.

(C) HPTLC assay showing a representative quantification of phosphatidylethanolamine (PE), PS, PI, and PC in WT and *pss1-3* seedlings.

(D) Table showing the percentage of the four major PS species in WT, *pss1-3*, and *pss1-4* quantified by LC-MS/MS. n.d., non-detected.

(E) Confocal images of *Arabidopsis* root epidermis expressing mCIT-C2^{LACT} and mCIT-2xPH^{EVCT2}, in WT, *pss1-3, pss1-3* supplemented with 54μM lyso-PS or lyso-PA for 60 min. Scale bars, 5 μm. See also Figure S3 and Table S1.

seedlings for 1 hour with lyso-PS, but not lyso-PA, fully complemented mCIT-C2^{LACT} fluorescence signal intensity and localization at the PM and intracellular compartments (Figure 3E). In addition, the mCIT-2xPH^{EVCT2} probe was fully cytosolic in *pss1-3*, as expected for a PS-depleted mutant and this localization was rescued by 1 hour lyso-PS but not lyso-PA treatment (Figure 3E). Furthermore, both root and shoot phenotypes were partially rescued by exogenous treatment with lyso-PS (Figures S3E–S3I). Together, our biochemical, cell biological, and phenotypical analyses suggest that *pss1-3* and *pss1-4* mutants do not produce any PS, which seems dispensable for gametogenesis and embryonic development but is absolutely required for normal post-embryonic plant development and sporophyte fertility. In addition, the *pss1* mutant further validates the specificity of our PS-binding probes C2^{LACT} and 2xPH^{EVCT2}.

PS Is Required for Surface Charges of the PM Cytosolic Leaflet

Next, we analyzed the localization of our membrane charge reporters in *pss1-3* mutant background. Both mCIT$^{8K-Farn}$ and mCIT-KA1^{MARK1} retained a certain degree of PM localization in *pss1-3*, but also relocalized in the cytosol and were found in intracellular compartments (Figures 4A and 4C). Quantification showed that the PM dissociation of mCIT-KA1^{MARK1} was weaker in *pss1-3* than upon PI4P depletion (i.e., PAO treatment), and similar as upon PA depletion (i.e., R59949) and was fully restored by short-term (1 hour) lyso-PS treatment (Figures 4A and 4C). Since we previously showed that PI4P and PA regulate PM electrostatics (Simon et al., 2016; Figure 1), we next asked whether loss of PS might affect PM anionic phospholipid subcellular distribution. Interestingly, the PM localization of PI(4,5)P_2, PI4P, and PA sensors were not affected in *pss1-3* (Figure 4D). In addition, by introgressing in *pss1-3* various control fluorescent markers of the PM (Figure 4B), and intracellular compartments (Figure S4), we could not detect any phenotype suggesting general defects in PM protein localization, membrane organization, and/or compartments morphogenesis. Taken together, our data indicate that loss of PS is the primary cause behind the PM electrostatic defects observed in *pss1*.

As described above, PS is presumably the last remaining anionic phospholipid at the PM following depletion of cellular PI4P/PI(4,5)P_2/PA using a combination of PAO and R59949 treatment. If this assumption is correct, the vast majority of anionic phospholipids should be removed from the PM in the *pss1* mutant following this treatment, which should therefore trigger a full dissociation from the PM of our mCIT-KA1^{MARK1} membrane charge reporter. Concomitant PAO/R59949 treatment in

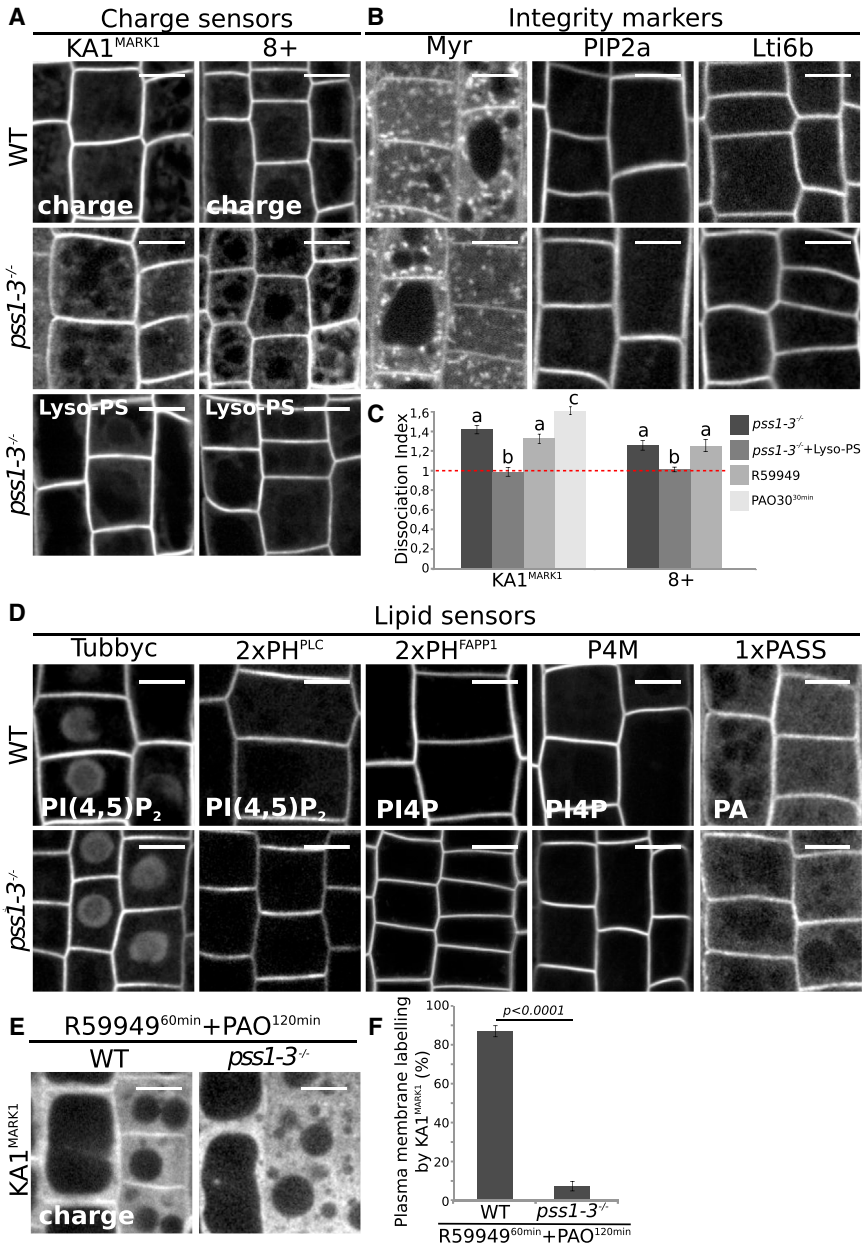

Figure 4. PS Contributes to PM Surface Charges but Is Not Required for the Localization of Other Anionic Phospholipids

(A) Confocal images of *Arabidopsis* root epidermis expressing, mCIT-KA1^{MARK1} or mCIT$^{8K-Farn}$ (8+) in WT, *pss1-3*, and *pss1-3* supplemented with 54 μM lyso-PS for 60 min.

(B) Confocal images of *Arabidopsis* root epidermis expressing mCIT/GFP-tagged PM integrity markers in WT and *pss1-3*.

(C) Quantification (mean ± SEM, n = 150 cells) of mCIT-KA1^{MARK1} and mCIT-8K^{Farn} (8+) dissociation index in *pss1-3*, *pss1-3* supplemented with 54 μM lyso-PS for 60 min, 12.5 μM R59949 for 60 min (same dataset as in Figure 1D), and 30 μM PAO for 30 min. Different letters indicate significant differences among means (p value = 0.05, Kruskal-Wallis bilateral test).

(D) Confocal images of *Arabidopsis* root epidermis expressing mCIT-tagged lipid sensors in WT and *pss1-3*.

(E) Confocal images of WT and *pss1-3* root epidermis expressing mCIT-KA1^{MARK1} pre-treated with 30 μM PAO for 60 min and then 12.5 μM R59949 and 30 μM PAO for 60 min.

(F) Quantification (mean ± SEM) of the percentage of cells with mCIT-KA1^{MARK1} at the PM in WT (n = 887cells) and *pss1-3* (n = 806 cells) (same treatment as in E). Statistical analysis was performed using the non-parametric Wilcoxon-Mann-Whitney test (p value = 0.05). Scale bars, 5 μm. See also Figure S4.

pss1-3, indeed induced a complete loss of PM localization of mCIT-KA1^{MARK1}, which became fully soluble in the cytosol (Figures 4E and 4F). This experiment demonstrates that PM localization of mCIT-KA1^{MARK1} in wild-type plants following concomitant PAO/R59949 treatment can be attributed to PS. Altogether, our results show that PS is not directly involved in the PM localization of other anionic lipids, but contribute to PM surface charges.

PS Sensor Localization Correlates with That of Electrostatic Compartments

We next asked whether PS could also participate in membrane surface charges of intracellular compartments. To this end, we mapped PS intracellular localization using quantitative colocalization analyses (see Figure S5 for a description of the method).

In accordance with the BFA and Wm sensitivity (Figure 2A), both the mCIT-C2^{LACT} and mCIT-2xPH^{EVCT2} probes localized in post-Golgi (p-G) compartments (Figures 5A and 5B). Interestingly, we found that both PS probes accumulated according to a concentration gradient, which is higher in early endocytic compartments (including EE/TGN and TGN-derived secretory vesicles [SV]), intermediate in the Golgi apparatus (Golgi) and lower in LEs (Figure 5B). Note that if there is a gradient of PS in endocytic compartments, the relative signal from the EE/TGN compartments should be greater than that of the LE compartments. Indeed, if a particular compartment has more available binding sites than another, it should not only increase the respective percentage of colocalization between the two markers, but also have higher signal intensity of the yellow marker in the red-labeled compartments with more binding sites. We therefore calculated the average fluorescence intensity of mCIT-C2^{LACT} in TGN/EE, SV, and LE, which confirmed that TGN/EE and SV contained quantitatively more mCIT-C2^{LACT} than LE (Figure 5C).

Next, we addressed which intracellular compartments were electronegative. To this end, we used charge reporters that are hydrophobically anchored to membrane via a farnesyl moiety and that have an adjacent unstructured peptide of net varying

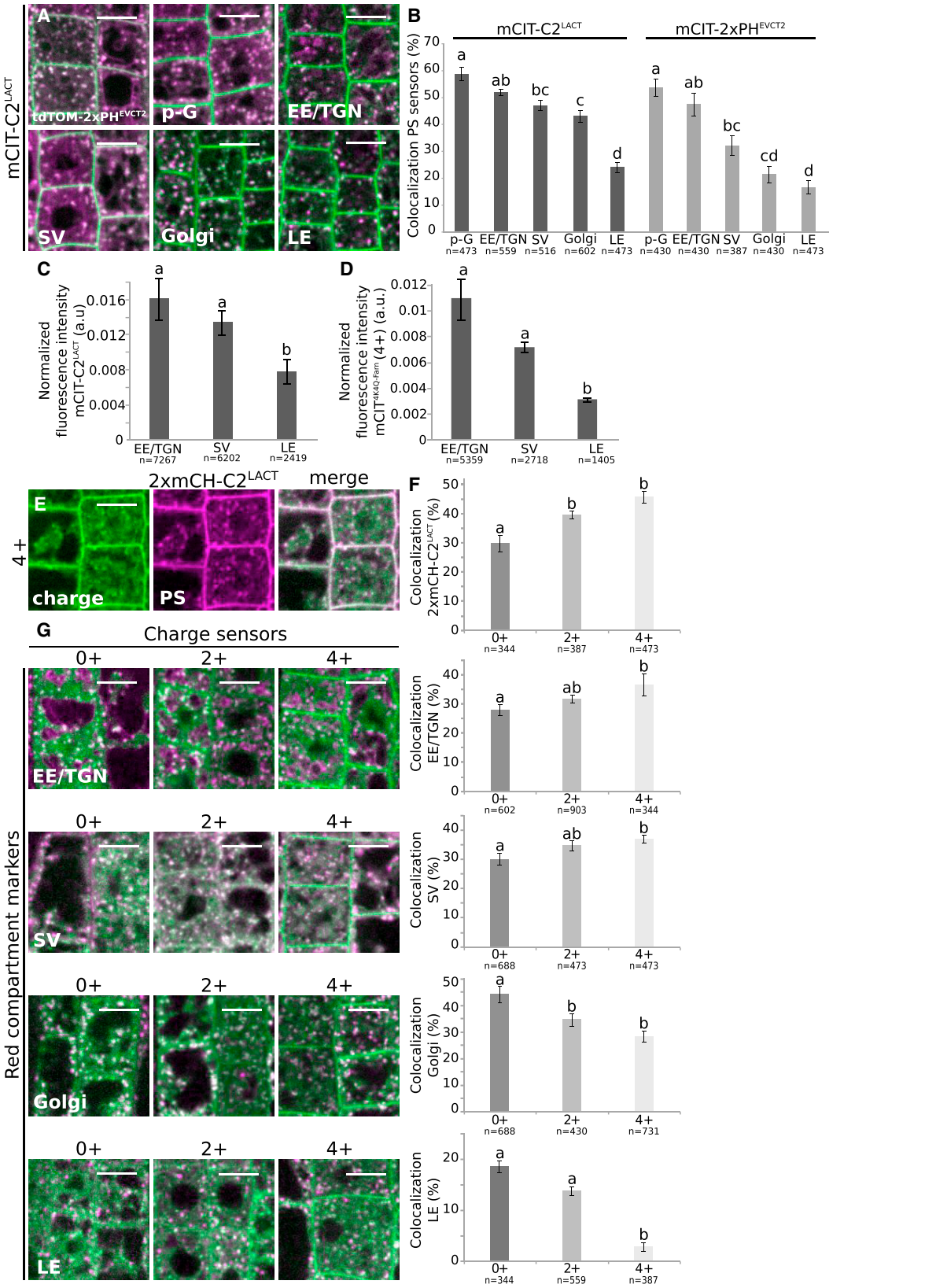

(legend on next page)

charges (from +0 to +8) (Simon et al., 2016). A neutral version of the probe (+0, 8Q-Farn) is localized only by the intrinsic properties of the farnesyl lipid anchor, independently of membrane electrostatics. The gradual addition of positive charges by substitution of neutral glutamines into cationic lysines gradually increases the avidity of the probes for anionic membranes. As a result, a probe with intermediate charges (e.g., 4K4Q-Farn, 4+) resides in compartments that are electronegative indistinctively of whether they are highly negatively charged or not (Yeung et al., 2006). By contrast, a probe that is strongly cationic (e.g., 8K-Farn, 8+) is greatly stabilized in highly anionic membranes such as the PM and is not found on compartments of intermediate electronegativity. We therefore reasoned that if PS contributes to the electrostatic properties of intracellular compartments, it should accumulate in compartments that are electronegative. Consistently, mCIT$^{4K4Q-Farn}$ (4+) preferentially accumulated in EE/TGN and SV rather than LE (Figure 5D), and extensively colocalized with the 2xmCH-C2^{LACT} PS sensor (Figure 5E). In addition, 2xmCH-C2^{LACT} colocalized preferentially with mCIT$^{4K4Q-Farn}$ (4+) (which labels electrostatic compartments) rather than mCIT$^{8Q-Farn}$ (0+) (the localization of which is charge independent) (Figure 5F). We next performed quantitative colocalization assays between intracellular compartment markers and charge reporters containing a gradual increase in net positive charges (0+, 2+, and 4+) in order to test the relative contribution of their positive charges on their intracellular distribution. Addition of positive charges gradually increased the proportion of the probes in EE/TGN and SV at the expense of their Golgi and LE localization (Figure 5G). Therefore, the endomembrane system is organized according to an electrostatic gradient that is the highest at the PM, intermediate in early endocytic compartments, and low in the Golgi and LEs. This electrostatic gradient correlates with the PS concentration gradient, which suggests that PS might be involved in defining this electrostatic territory.

Membrane Surface Charge Probes Relocalize to EE/TGN upon Disruption of PM Electrostatics

Next, to test whether intracellular PS could control the electrostatic properties of intracellular membrane compartments, we inhibited PI4P synthesis using a 30-min PAO treatment (Simon et al., 2016) and asked where the mCIT$^{8K-Farn}$ (8+) relocalized inside the cell. Interestingly, following PAO treatment, mCIT$^{8K-Farn}$ was observed on the surface of PS-bearing organelles (Figure 6A), being mainly localized in EE/TGN and SV (Figures 6B and S6A–S6C). As an alternative to PAO treatment, we also specifically depleted PI4P at the PM using a PM-targeted 4-phosphatase (i.e., the catalytic domain of the yeast Sac1p PI4P phosphatase) in *Nicotiana benthamiana* leaves (Simon et al., 2016). PI4P depletion at the PM triggers the redistribution of the 2xmCH-KA1^{MARK1} charge sensor in PS-bearing compartments, as determined by the presence of mCIT-C2^{Lact} and mCIT-2xPH^{EVTC2} (Figures 6C and S6D). These results suggest that in the absence of PI4P, which is required for the distinctively high PM electrostatic signature (Simon et al., 2016), strongly cationic membrane surface charge reporters (such as the mCIT$^{8K-Farn}$ or mCIT-KA1^{MARK1} reporters) localize inside the cell according to the PS concentration gradient.

We previously noticed that PI4-kinase inhibition by PAO affects PS intracellular distribution (Simon et al., 2016). We therefore analyzed quantitatively PS subcellular localization in the absence or presence of PAO. PAO treatment attenuated the gradient of PS as visualized by mCIT-C2^{LACT} (Figure 6F). In particular, it increased the localization of mCIT-C2^{LACT} in LE (Figures 6E and 6F). Strikingly, the electrostatic gradient, as visualized by the mCIT$^{4K4Q-Farn}$ (4+) charge reporter was similarly affected by PAO treatment, with an increased localization of the reporter in LE (Figures 6G, 6H, and S6E–S6H). These results confirm that charge reporter localization coincides with the presence of PS at the surface of intracellular membranes. In addition, we also noticed that PAO treatment decreased the accumulation of the mCIT$^{4K4Q-Farn}$ (4+) probe in EE/TGN (Figure 6H), while PS localization in this compartment was only mildly affected by this treatment (Figure 6F). PAO affects PI4P production, a lipid that is present in EE/TGN albeit to a lower extent than the PM (Simon et al., 2016). Loss of PI4P may therefore impact the electrostatic properties of EE/TGN and may explain the decreased accumulation of the mCIT$^{4K4Q-Farn}$ (4+) probe in this compartment. As such, PI4P likely acts in combination with PS to specify the intermediate electronegativity of EE/TGN. Accordingly, 2xmCH-KA1^{MARK1} relocalizes to PI4P-containing endosomes upon PI4P depletion at the PM in *N. benthamiana*, as visualized by its colocalization with the PI4P reporter, mCIT-P4M^{SiDM} (Figure 6D).

Figure 5. A PS Gradient along the Endocytic Pathway Correlates with a Gradient of Electrostatics

(A) Merged confocal images of *Arabidopsis* root epidermis of plants co-expressing mCIT-C2^{LACT} (PS, green) with tdTOMATO-2xPH^{EVCT2} (PS), W25R post-Golgi marker (p-G), W13R early endosomal marker (EE/TGN), W24R SV marker (SV), W18R Golgi marker, W7R late endosomal marker (LE) in magenta.

(B) Quantification of the percentage of compartments labeled by PS sensors that also contain compartment markers (same as above-mentioned), n = (387, 602) cells (mean ± SEM, percentage of colocalization). Different letters indicate significant differences among means (p value = 0.05, Kruskal-Wallis bilateral test).

(C and D) Quantification (mean ± SEM) of the fluorescence intensity of mCIT-C2^{LACT} (C) and mCIT$^{4K4Q-Farn}$ (D), which colocalize with W13R (EE/TGN), W24R (SV), and W7R (LE) and normalized over the total fluorescent intensity of each picture, n = (1405; 7264) colocalizing spots. Different letters indicate significant differences among means (p value = 0.05, Kruskal-Wallis bilateral test).

(E) Confocal images of plants co-expressing mCIT$^{4K4Q-Farn}$ (4+, green) and 2xmCH-C2^{LACT} (PS, magenta).

(F) Quantification (mean ± SEM) of the percentage of compartments labeled by PS sensors (2xmCH-C2^{LACT}) that also contain membrane charge reporters (mCIT$^{8Q-Farn}$ [0+], 2xmCIT$^{2K6Q-Farn}$ [2+], and 2xmCIT$^{4K4Q-Farn}$ [4+]), n = (387, 602) cells. Different letters indicate significant differences among means (p value = 0.05, Kruskal-Wallis bilateral test),

(G) Merged confocal images (left) and colocalization quantification (mean ± SEM) of plants co-expressing mCIT$^{8Q-Farn}$ (0+), mCIT$^{2K6Q-Farn}$ (2+), and mCIT$^{4K4Q-Farn}$ (4+) in green, with W13R (EE/TGN), W24R (SV), W18R (Golgi), and W7R (LE) markers in magenta, n = (344, 688) cells. Different letters indicate significant differences among means (p value = 0.15, Kruskal-Wallis bilateral test). In graphs (B), (F), and (G), "n" represents the estimated number of cells sampled in each condition, in graphs (C) and (D), "n" represents the number of colocalizing spots analyzed in each condition. Scale bars, 5 μm.

See also Figure S5.

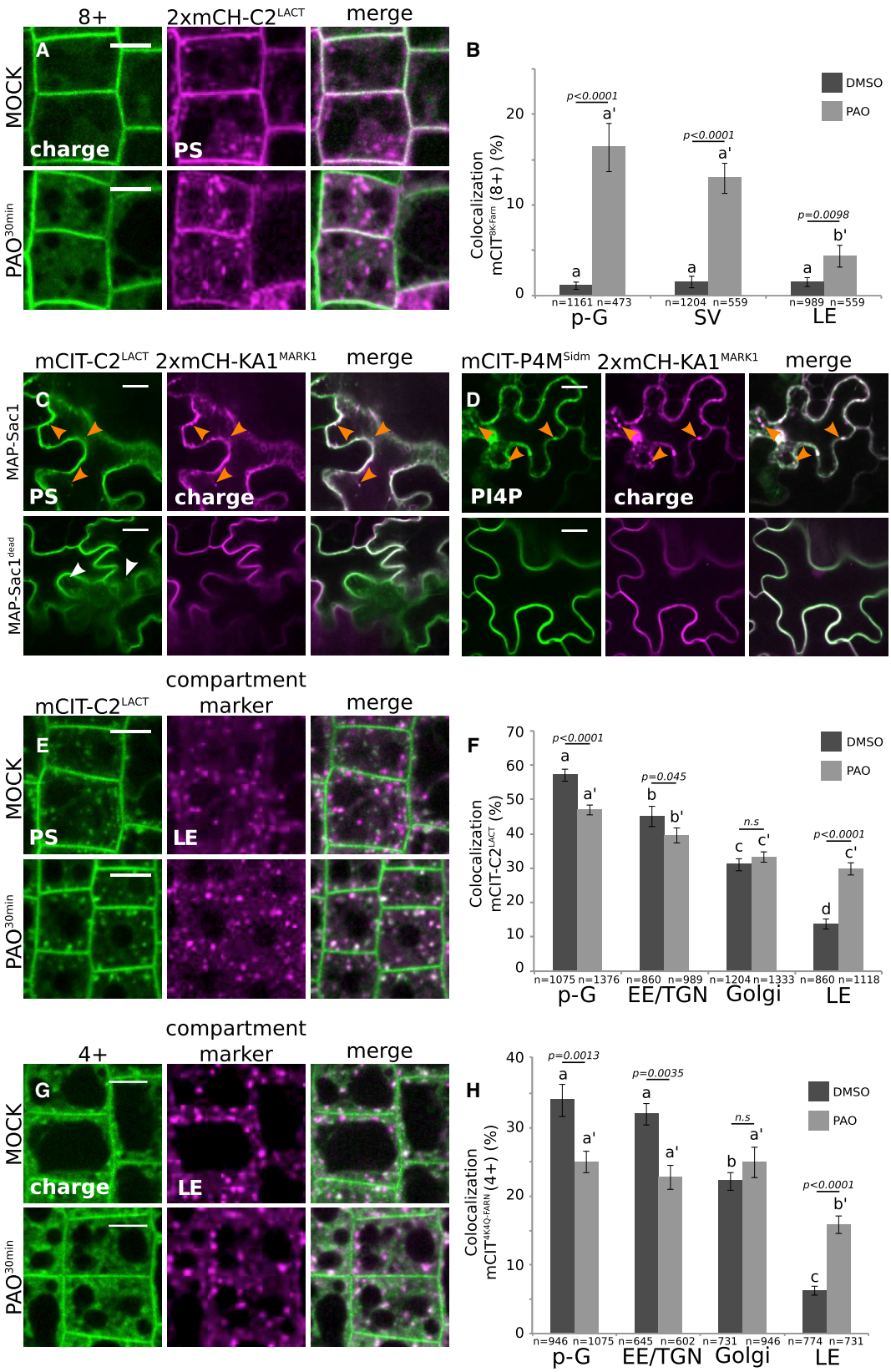

(legend on next page)

Membrane Electrostatics, Together with Curvature, Acts as a Targeting Signal to EE/TGN Compartments

We next designed a new sensor able to report on the electrostatic properties of EE/TGN without the need to alter the PM lipid composition. To this end, we fused mCIT to the +ALPS motif of the yeast Gcs1p protein (+ALPS^{GCS1}-mCIT) and expressed it stably in *Arabidopsis* (Figures 7A and 7B). ALPS (Amphipathic Lipid Packing Sensor) motifs are particular amphipathic α-helices with a weakly charged serine-threonine-rich polar face that recognize packing defects that are found in curved membranes (Bigay and Antonny, 2012). These motifs usually localize in ER or Golgi membranes, known to have a higher occurrence of packing defects. However, a subset of ALPS motifs has an adjacent stretch with few cationic residues (so-called +ALPS), that were shown in the case of Gcs1p to drive its localization beyond the Golgi into the TGN, in a charge-dependent manner (Xu et al., 2013). Altogether, the localization of the +ALPS motifs relies on the coincident detection of curved-electrostatic membranes (Figure 7A). We found that +ALPS^{GCS1}-mCIT extensively colocalized with 2xmCH-C2^{Lact} and 2xmCH-1xPH^{FAPP1}, suggesting that it resides in PS and PI4P-containing endosomes and therefore indeed localize to electrostatic compartments (Figure 7B). To test the importance of the charges in +ALPS^{GCS1}-mCIT localization, we expressed a mutated version of the +ALPS motif, +ALPS^{K210Q}-mCIT, in which K210, a critical lysine residue for interaction with anionic membranes (Xu et al., 2013), was substituted with a neutral glutamine (Figure 7A). Reducing the charge of the +ALPS motif concomitantly diminished the localization of +ALPS^{GCS1}-mCIT in the EE/TGN (more particularly the SV subset of the EE/TGN) and increased its localization in the Golgi apparatus, while having no effect on its weak association with LEs (Figures 7C and 7D). In addition, inhibition of either PI4P or PS biosynthesis, using PAO or the *pss1* mutant, respectively, reduced the colocalization between +ALPS^{GCS1}-mCIT and a marker of the SV subset of the EE/TGN (Figures 7E and 7F). Together, these results support a role for electrostatic interactions in targeting this +ALPS motif to the EE/TGN *in planta* and confirm the importance of both PI4P and PS in driving the electrostatic properties of this compartment.

Next, we asked whether the curved/electrostatic properties of the EE/TGN could be important to target endogenous plant proteins to this compartment. To this end, we mined the *Arabidopsis* proteome for proteins that would contain both an ALPS motif, as well as an adjacent positive stretch of amino acids (Gautier et al., 2008). We found that the PI4-kinaseβ1 and PI4Kβ2, as well as the ARF-GAP proteins AGD6 and AGD7, harbor a putative +ALPS motif(s) (Figures 7G, 7H, and S7A–S7C). PI4Kβ1 was shown to reside in the SV subset of the EE/TGN (Kang et al., 2011; Preuss et al., 2006). In order to probe the function of the +ALPS motif in PI4Kβ1 localization, we expressed full-length mCIT-PI4Kβ1, as well as a mutated version without the +ALPS motifs (mCIT-PI4Kβ1$^{\Delta+ALPS}$) or the +ALPS motif alone (mCIT + ALPS$^{PI4K\beta1}$) in *N. benthamiana* leaves (Figure 7I). Both mCIT-PI4Kβ1 and mCIT+ALPS$^{PI4K\beta1}$ localized in intracellular compartments in this system, while mCIT-PI4Kβ1$^{\Delta+ALPS}$ was soluble (Figure 7I). These data suggest that the +ALPS motif of PI4Kβ1 is necessary and sufficient to target this protein to intracellular compartments and therefore likely contributes to its localization into SV. Similarly, wild-type AGD6-mCIT was targeted to intracellular compartments in *N. benthamiana* leaves but not a mutant version in its +ALPS motif (Figure S7D). Together, our results suggest that +ALPS-containing proteins may rely on the coincident detection of both the electrostatic and curvature properties of the EE/TGN compartment for localization.

DISCUSSION

Here, we addressed which organelles comprise the electrostatic territory in plants and what are the anionic lipids that control this territory. Similar to previously published models, we find that the plant electrostatic territory corresponds to PM-derived organelles (Bigay and Antonny, 2012). However, interestingly, we noticed that not all membranes in this territory are equally anionic. Rather, we revealed the existence of an electrostatic gradient, which is at its highest at the PM, intermediate in early endosomes and low in LEs. This electrostatic gradient is set up by various anionic phospholipid combinations. The concomitant

Figure 6. PS and PI4P Cooperate to Control Endosome Electrostatics

(A) Confocal images of plants co-expressing mCIT$^{8K-Farn}$ (8+, green) with mCh-C2^{LACT} (PS, magenta) in mock and PAO (60μM, 30 min) conditions.

(B) Quantification (mean ± SEM) of the percentage of compartments labeled by mCIT$^{8K-Farn}$ (8+) that also contain W25R (p-G), W24R (SV), and W7R (LE) in the presence or absence of PAO (60 μM, 30 min) n = (478, 1,204) cells.

(C) Confocal images of mCIT-C2^{Lact} (PS, green), 2xmCH-KA1^{MARK1} (charges, magenta), and corresponding merge in *N. benthamiana* epidermal cell transiently co-transfected with MAP-Sac1-mTURQUOISE2 or MAP-Sac1^{DEAD}-mTURQUOISE2. Orange arrowheads indicate colocalization between C2^{Lact} and KA1^{MARK1}-containing endosomes in the presence of MAP-Sac1, and white arrowheads indicates endosomes containing only C2^{Lact} but not KA1^{MARK1} in the presence of MAP-Sac1^{DEAD}.

(D) Confocal images of mCIT-P4M^{SiDM} (PI4P, green), 2xmCH-KA1^{MARK1} (charges, magenta) and corresponding merge in *N. benthamiana* epidermal cell transiently co-transfected with MAP-Sac1-mTURQUOISE2 or MAP-Sac1^{DEAD}-mTURQUOISE2. Orange arrows indicate colocalization between P4M^{SiDM} and KA1^{MARK1}-containing endosomes in the presence of MAP-Sac1.

(E) Confocal images of plants co-expressing mCIT-C2^{LACT} (PS, green) with W7R (LE, magenta) in mock and PAO (60μM, 30 min) conditions.

(F) Quantification (mean ± SEM) of the percentage of compartments labeled by mCIT-C2^{LACT} that also contain W25R (p-G), W13R (EE/TGN), W18R (Golgi), and W7R (LE) in the presence or absence of PAO (60 μM, 30 min), n = (860, 1,376 cells).

(G) Confocal images of plants co-expressing mCIT$^{4K4Q-Farn}$ (4+, green) with W7R (LE, magenta) in mock and PAO (60 μM, 30 min) conditions.

(H) Quantification (mean ± SEM) of the percentage of compartments labeled by mCIT$^{4K4Q-Farn}$ (4+), that also contain W25R (p-G) W13R (EE/TGN), W18R (Golgi), and W7R (LE) in the presence or absence of PAO (60 μM, 30 min), n = (602, 1,075) cells. In graphs (B), (F), and (H), different letters indicate significant differences among means (normal letters for DMSO comparison and letters with a prime symbol for PAO comparison, p value = 0.05, Kruskal-Wallis bilateral test). Statistical difference between each sample is indicated by the p value at the top of each compared conditions (p value = 0.05, non-parametric Wilcoxon-Mann-Whitney test, non-significant [n.s]). "n" represents the estimated number of cells sampled in each condition. Scale bars, 5 μm.

See also Figure S6.

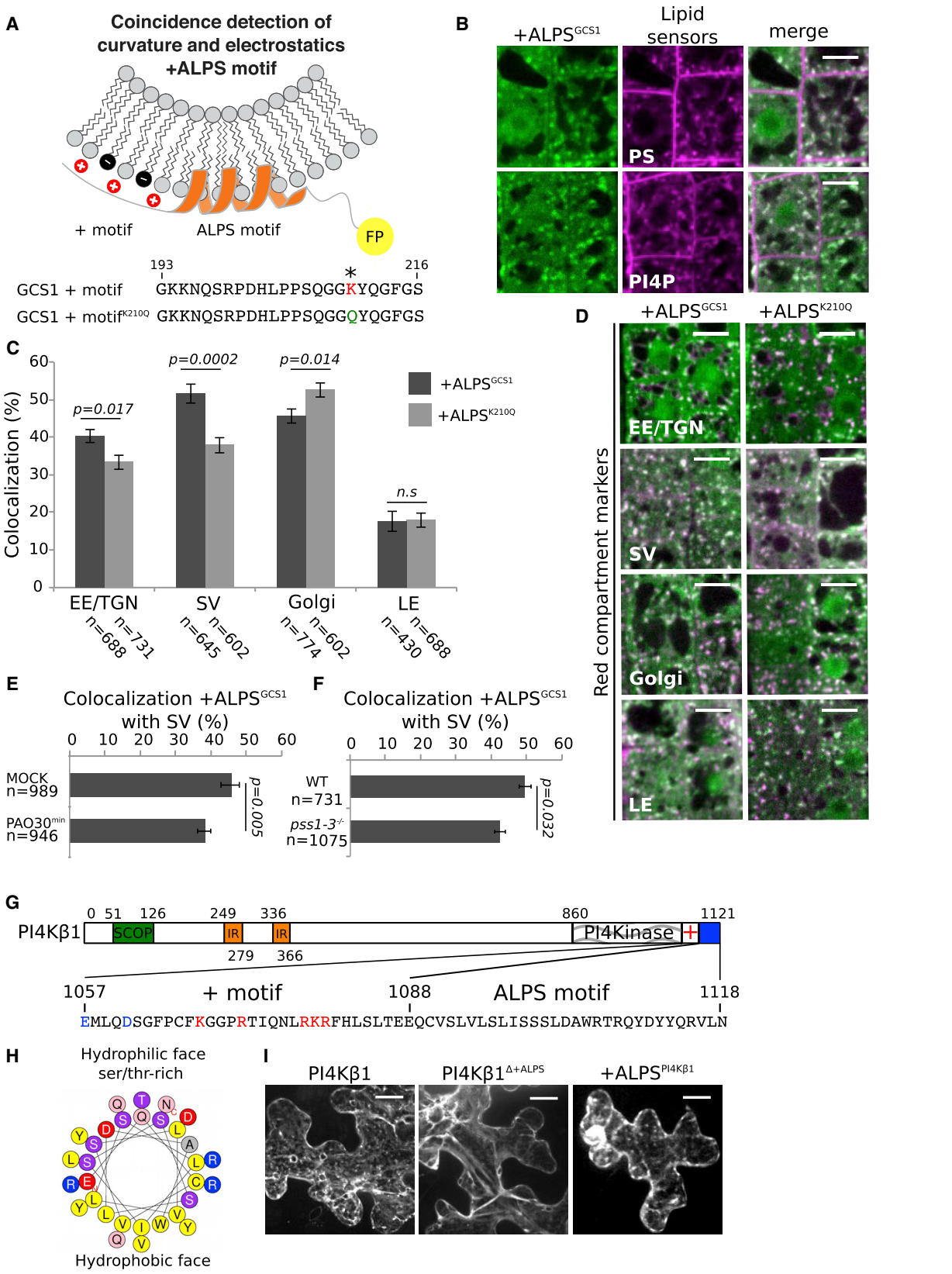

(legend on next page)

accumulation of PI4P, PA, and PS drives the very high electrostatic field of the PM. However, PS accumulation extends beyond the PM as it accumulates along the endocytic pathway according to a concentration gradient, suggesting that PS is likely instrumental in setting up the electrostatic territory. In this scenario, PS and PI4P, which are found in the EE/TGN, drive the intermediate electrostatic properties of this compartment.

An Electrostatic Gradient along the Plant Endocytic Pathway Contributes to Protein Localization

The existence of this electrostatic gradient may have several consequences on the organization of the plant endomembrane system. First, electrostatic membranes seem to be a hallmark of PM-derived organelles (Bigay and Antonny, 2012). As such, proteins with polybasic regions or cationic domains are likely to localize in this territory. Furthermore, because it is organized as a concentration gradient, membrane electrostatics may also contribute to the specific targeting of proteins to different organelles within the electrostatic territory. For example, proteins that have highly cationic motifs (net positive charges of 6 or more) are likely to be specifically targeted to the plant PM, because it is by far the most electronegative cellular membrane (Simon et al., 2016). This is, for example, the case of the BRI1 KINASE INHIBITOR1 (BKI1) or the AGC kinases PINOID and D6-PROTEIN KINASE (D6PK), which are involved in brassinosteroid and polar auxin transport regulation, respectively (Barbosa et al., 2016; Simon et al., 2016). By contrast, proteins with slightly less cationic regions might be targeted to additional organelles, in particular EE/TGN, as exemplified by the 4K4Q-Farn (+4) charge reporter. For example, in animal cells, c-Src localizes to both the PM and endosomes and has a polybasic stretch of +5 adjacent to its myristoylation anchor (Yeung et al., 2008). In addition, we propose that the coincident detection of negative charges and curvature at the EE/TGN acts as a determinant of +ALPS-containing protein localization. Importantly, the net positive charges adjacent to the ALPS motifs only range from +1 to +3, which by itself would not be sufficient for membrane targeting by electrostatic interactions. However, in the context of coincident detection with curved membranes, these few positive charges are enough to contribute to localization specificity. In addition, proteins may be targeted to EE/TGN by a combination of non-specific electrostatic interactions with anionic membranes and concomitant binding with a specific protein or lipid in a given compartment. Altogether, we propose that the electrostatic gradient found along the endocytic pathway may be one of the fundamental properties that localizes soluble proteins to PM-derived organelles in plants.

Role of the Different Anionic Lipids in the Electrostatic Landscape of Plant Membranes

In mammalian cells, PS is enriched in PM-derived organelles and was proposed to act as a landmark of the electrostatic territory (Bigay and Antonny, 2012; Yeung et al., 2008). Here, we combined pharmacological and genetic approaches to demonstrate that in plants, PS is both necessary to establish the PM electrostatic signature, and sufficient to maintain a certain degree of surface charges at the PM. In addition, we show that PS does not act alone in this process but rather do so in concert with PI4P and PA. With this respect, our work exemplifies the non-linear relationship between anionic lipid quantity and their respective impact on membrane electrostatics. Indeed, while PS is present in much higher quantity than PI4P, we found that the latter has a stronger impact on the PM electrostatic signature. On the other hand, PS seems to have a relatively modest effect on PM electrostatics, and to be more important for the definition of the electrostatic territory overall.

We also found an unexpected role for PA in PM electrostatics, which was not previously reported in other organisms. In animals, most cells have a minute amount of PA at the PM, and PA sensors are not recruited to the PM in resting conditions (Bohdanowicz et al., 2013). Interestingly, in the present study, we show that the plant PM has significant PA levels, as visualized by the recruitment of PA-binding sensors, even when plants are grown in optimal conditions (i.e., independent of stress-induced PA production). This finding is in line with the high levels of PA found by direct biochemical measurements in PM fraction of several plant species, including *Arabidopsis*, which were shown to range from 3% to 20% of total phospholipid (Moreau et al., 1998; Uemura et al., 1995). It was recently shown that PA plays a role in the PM targeting of D6PK (Barbosa et al., 2016). The localization of D6PK is dependent on PI4P, PI(4,5)P_2, and PA, suggesting that a combination of phosphoinositides and PA is

Figure 7. Endosome Electrostatics Is Required to Promote + ALPS-Containing Protein Localization at the EE/TGN

(A) Schematic representation of the coincident detection of membrane electrostatics and curvature by +ALPS motif and sequence of polybasic stretch adjacent to the ALPS motif of the yeast Gcs1p protein. *: critical lysine residue for interaction with anionic lipids.

(B) Confocal images of plants co-expressing +ALPS^{GCS1}-mCIT (green) with 2xmCH-C2^{LACT} (PS, magenta) or 2xmCH-1xPH^{FAPP1} (PI4P, magenta).

(C and D) Quantification (mean ± SEM) of the percentage of compartments labeled by +ALPS^{GCS1}-mCIT or +ALPS^{K210Q}-mCIT, that also contain W13R (EE/TGN), W24R (SV), W18R (Golgi), and W7R (LE), n = (430, 774) cells and (D), corresponding merged confocal pictures with +ALPS^{GCS1}-mCIT and +ALPS^{K210Q}-mCIT in green and compartment markers in magenta.

(E) Quantification (mean ± SEM) of the percentage of compartments labeled by +ALPS^{GCS1}-mCIT that also contain W24R (SV) in the mock and PAO (30 min, 30 μM) treated conditions, n = (946, 989) cells.

(F) Quantification (mean ± SEM) of the percentage of compartments labeled by +ALPS^{GCS1}-mCIT that also contain W24R (SV) in the WT and *pss1-3* mutant, n = (731, 1,075) cells.

(G) Schematic representation of PI4Kβ1 protein structural organization with the corresponding sequence of its C-terminal +ALPS motif. SCOP, SCOP domain; IR, internal repeat.

(H) Helical wheel representation the PI4Kβ1 ALPS motif.

(I) Confocal images of mCIT-PI4Kβ1, mCIT-PI4Kβ1$^{\Delta+ALPS}$, and mCIT + ALPS$^{PI4K\beta1}$ in *N. benthamiana* leaf epidermal cells. In graphs (C) and (E), statistical difference between each sample is indicated by the p value at the top of each compared conditions (p value = 0.05, non-parametric Wilcoxon-Mann-Whitney test, non-significant [n.s]). "n" represents the estimated number of cells sampled in each condition. Scale bars, 5 μm, except in (I), 50 μm.

See also Figure S7.

responsible for its localization rather than a single phospholipid species (Barbosa et al., 2016). Here, we obtained similar results with several independent generic membrane surface charge reporters, suggesting that the requirement for multiple anionic phospholipids may not be an intrinsic property of D6PK but rather a more general feature of the electrostatic field of the plant PM. In addition, this further suggests that our results are not limited to our synthetic charge reporters, but are relevant for the localization of endogenous *Arabidopsis* proteins, and point toward a more general requirement of PI4P/PA/PS combination for the localization of many proteins in plants. However, it is worth mentioning that the localization of D6PK is not identical to that of generic membrane surface charge sensors. Indeed, unlike these sensors (Simon et al., 2016), D6PK localizes at the basal pole of the cell (Barbosa et al., 2016). It is therefore likely that D6PK localization is regulated by additional factors, which might include PI(4,5)P_2 as well as other, yet unknown regulators.

In plants, we found that the individual loss of PI4P, PA, and PS directly impacts PM electrostatics. One may speculate that spatiotemporal variations in PI4P, PA, and/or PS may directly impact PM surface charges. As such, PM electrostatics in plants may be particularly prone to responding to developmental and environmental cues. It will be an exciting future direction to understand how these different signals may impact membrane electrostatics, what are the contributions of individual lipid species in these variations, and how this might regulate signaling, intracellular trafficking, and cellular polarity.

STAR★METHODS

Detailed methods are provided in the online version of this paper and include the following:

- KEY RESOURCES TABLE
- CONTACT FOR REAGENT AND RESOURCE SHARING
- EXPERIMENTAL MODEL AND SUBJECT DETAILS
  - Growth Condition and Plant Materials
  - Plant Transformation and Selection
  - Yeast
- METHOD DETAILS
  - Microscopy Setup
  - Time Lapse Imaging
  - Shoot Apical Meristem Imaging
  - FM4-64, BFA, WM, PAO, R59022, R59949 and Cold Treatments
  - Dissociation Index
  - Subcellular and Phenotype Complementation with Lysophospholipids
  - Colocalization Analyses
  - Quantification of Normalized Fluorescence Intensity in Colocalizing Spots
  - ALPS Motif Detection and Representation
  - Genotyping and Characterization of *pss1* T-DNA Insertion Lines
  - Quantification of the Root Length and Root Growth Rate
  - Quantification of the Rosette Area
  - Cloning
  - *In vitro* Assay
  - Lipid Quantification for Lipid Measurement in *pss1* Mutant (HPTLC and LC-MS/MS)
  - Lipid Quantification for R59949 and R59022 Treatment (HPTLC)
- QUANTIFICATION AND STATISTICAL ANALYSIS

SUPPLEMENTAL INFORMATION

Supplemental Information includes seven figures, two tables, and five videos and can be found with this article online at https://doi.org/10.1016/j.devcel.2018.04.011.

ACKNOWLEDGMENTS

We thank A. Martinière-Delaunay, O. Hamant, M. Dreux, and the SiCE group for discussions and comments; G. Du, T. Taguchi, S. Grinstein, B. Kost, T. Graham, and addgene for providing plasmids; N. Geldner, K. Schumacher, I. Moore, D. Ehrhardt, the GABI-KAT, and the NASC collection for providing transgenic *Arabidopsis* lines; A. Lacroix, J. Berger, and P. Bolland for plant care; J.C. Mulatier for help in preparing lipids. We acknowledge the contribution of SFR Biosciences (UMS3444/CNRS, US8/Inserm, ENS de Lyon, UCBL) facilities: C. Lionet and C. Chamot at the LBI-PLATIM-MICROSCOPY for assistance with imaging. Y.J. is funded by ERC no. 3363360-APPL under FP/2007–2013. L.C.N., M.D., and M.S. are funded by PhD fellowships from the French Ministry of Higher Education. T.S. is supported by ERC grant no. 615739-MechanoDevo to O. Hamant. P.P. and M.P. are supported by the Czech Science Foundation grant no. 17-27477S. Lipidomic analyses were performed on the Bordeaux Metabolome Facility-MetaboHUB (ANR-11-INBS-0010).

AUTHOR CONTRIBUTIONS

M.P.P. was responsible for all experiments described in the manuscript except the following: production and imaging of the *PDF1*-driven PS reporter line (T.S.), lipid measurements (L.M.-P., L.F., and P.M.); time-lapse imaging of cytokinesis/root hair (M.D. and M.C.C.) and pollen tube (P.P. and M.P.); transient expression in *N. benthamiana* (M.D. and L.C.N.). L.C.N. cloned PI4Kβ1 and AGD6 constructs and imaged them. V.B. helped with image quantification and acquisition; L.A. helped with yeast and lipid overlay experiments; A.C. helped with lyso-PS/lyso-PA add-back experiments and amphipathic helix analyses; M.L.A.S. participated in the production of membrane charge reporter lines. M.P.P. and Y.J. conceived the study, designed experiments, and wrote the manuscript, and all the authors discussed the results and commented on the manuscript.

DECLARATION OF INTERESTS

The authors declare no competing interests.

Received: July 27, 2017
Revised: March 6, 2018
Accepted: April 11, 2018
Published: May 10, 2018

REFERENCES

Alberti, S., Gitler, A.D., and Lindquist, S. (2007). A suite of Gateway cloning vectors for high-throughput genetic analysis in Saccharomyces cerevisiae. Yeast *24*, 913–919.

Barbosa, I.C., Shikata, H., Zourelidou, M., Heilmann, M., Heilmann, I., and Schwechheimer, C. (2016). Phospholipid composition and a polybasic motif determine D6 PROTEIN KINASE polar association with the plasma membrane and tropic responses. Development *143*, 4687–4700.

Bayle, V., Platre, M.P., and Jaillais, Y. (2017). Automatic quantification of the number of intracellular compartments in *Arabidopsis thaliana* root cells. Bio Protoc. *7*, e2145.

Bigay, J., and Antonny, B. (2012). Curvature, lipid packing, and electrostatics of membrane organelles: defining cellular territories in determining specificity. Dev. Cell *23*, 886–895.

Bohdanowicz, M., Schlam, D., Hermansson, M., Rizzuti, D., Fairn, G.D., Ueyama, T., Somerharju, P., Du, G., and Grinstein, S. (2013). Phosphatidic acid is required for the constitutive ruffling and macropinocytosis of phagocytes. Mol. Biol. Cell *24*, 1700–1712, S1701-1707.

Bolte, S., and Cordelieres, F.P. (2006). A guided tour into subcellular colocalization analysis in light microscopy. J. Microsc. *224*, 213–232.

Chung, J., Torta, F., Masai, K., Lucast, L., Czapla, H., Tanner, L.B., Narayanaswamy, P., Wenk, M.R., Nakatsu, F., and De Camilli, P. (2015). INTRACELLULAR TRANSPORT. PI4P/phosphatidylserine countertransport at ORP5- and ORP8-mediated ER-plasma membrane contacts. Science *349*, 428–432.

Cutler, S.R., Ehrhardt, D.W., Griffitts, J.S., and Somerville, C.R. (2000). Random GFP::cDNA fusions enable visualization of subcellular structures in cells of *Arabidopsis* at a high frequency. Proc. Natl. Acad. Sci. USA *97*, 3718–3723.

Dettmer, J., Hong-Hermesdorf, A., Stierhof, Y.D., and Schumacher, K. (2006). Vacuolar H+-ATPase activity is required for endocytic and secretory trafficking in *Arabidopsis*. Plant Cell *18*, 715–730.

Doumane, M., Lionnet, C., Bayle, V., Jaillais, Y., and Caillaud, M.C. (2017). Automated tracking of root for confocal time-lapse imaging of cellular processes. Bio Protoc. *7*, e2245.

Elsayad, K., Werner, S., Gallemi, M., Kong, J., Sanchez Guajardo, E.R., Zhang, L., Jaillais, Y., Greb, T., and Belkhadir, Y. (2016). Mapping the subcellular mechanical properties of live cells in tissues with fluorescence emission-Brillouin imaging. Sci. Signal. *9*, rs5.

Fairn, G.D., Schieber, N.L., Ariotti, N., Murphy, S., Kuerschner, L., Webb, R.I., Grinstein, S., and Parton, R.G. (2011). High-resolution mapping reveals topologically distinct cellular pools of phosphatidylserine. J. Cell Biol. *194*, 257–275.

French, A., Ubeda-Tomas, S., Holman, T.J., Bennett, M.J., and Pridmore, T. (2009). High-throughput quantification of root growth using a novel image-analysis tool. Plant Physiol. *150*, 1784–1795.

Gautier, R., Douguet, D., Antonny, B., and Drin, G. (2008). HELIQUEST: a web server to screen sequences with specific alpha-helical properties. Bioinformatics *24*, 2101–2102.

Geldner, N., Denervaud-Tendon, V., Hyman, D.L., Mayer, U., Stierhof, Y.D., and Chory, J. (2009). Rapid, combinatorial analysis of membrane compartments in intact plants with a multicolor marker set. Plant J. *59*, 169–178.

Gietz, R.D., Schiestl, R.H., Willems, A.R., and Woods, R.A. (1995). Studies on the transformation of intact yeast cells by the LiAc/SS-DNA/PEG procedure. Yeast *11*, 355–360.

Gomez-Merino, F.C., Arana-Ceballos, F.A., Trejo-Tellez, L.I., Skirycz, A., Brearley, C.A., Dormann, P., and Mueller-Roeber, B. (2005). Arabidopsis AtDGK7, the smallest member of plant diacylglycerol kinases (DGKs), displays unique biochemical features and saturates at low substrate concentration: the DGK inhibitor R59022 differentially affects AtDGK2 and AtDGK7 activity in vitro and alters plant growth and development. J. Biol. Chem. *280*, 34888–34899.

Heape, A.M., Juguelin, H., Boiron, F., and Cassagne, C. (1985). Improved one-dimensional thin-layer chromatographic technique for polar lipids. J. Chromatogr. *322*, 391–395.

Jaillais, Y., Hothorn, M., Belkhadir, Y., Dabi, T., Nimchuk, Z.L., Meyerowitz, E.M., and Chory, J. (2011). Tyrosine phosphorylation controls brassinosteroid receptor activation by triggering membrane release of its kinase inhibitor. Genes Dev. *25*, 232–237.

Kang, B.H., Nielsen, E., Preuss, M.L., Mastronarde, D., and Staehelin, L.A. (2011). Electron tomography of RabA4b- and PI-4Kbeta1-labeled trans Golgi network compartments in *Arabidopsis*. Traffic *12*, 313–329.

Karimi, M., Bleys, A., Vanderhaeghen, R., and Hilson, P. (2007). Building blocks for plant gene assembly. Plant Physiol. *145*, 1183–1191.

Kleinboelting, N., Huep, G., Kloetgen, A., Viehoever, P., and Weisshaar, B. (2012). GABI-Kat SimpleSearch: new features of the *Arabidopsis thaliana* T-DNA mutant database. Nucleic Acids Res. *40*, D1211–D1215.

Kriechbaumer, V., Maneta-Peyret, L., Fouillen, L., Botchway, S.W., Upson, J., Hughes, L., Richardson, J., Kittelmann, M., Moreau, P., and Hawes, C. (2018). The odd one out: *Arabidopsis* reticulon 20 does not bend ER membranes but has a role in lipid regulation. Sci. Rep. *8*, 2310.

Laloi, M., Perret, A.M., Chatre, L., Melser, S., Cantrel, C., Vaultier, M.N., Zachowski, A., Bathany, K., Schmitter, J.M., Vallet, M., et al. (2007). Insights into the role of specific lipids in the formation and delivery of lipid microdomains to the plasma membrane of plant cells. Plant Physiol. *143*, 461–472.

Li, L., Shi, X., Guo, X., Li, H., and Xu, C. (2014). Ionic protein-lipid interaction at the plasma membrane: what can the charge do? Trends Biochem. Sci. *39*, 130–140.

Macala, L.J., Yu, R.K., and Ando, S. (1983). Analysis of brain lipids by high performance thin-layer chromatography and densitometry. J. Lipid Res. *24*, 1243–1250.

Maeda, K., Anand, K., Chiapparino, A., Kumar, A., Poletto, M., Kaksonen, M., and Gavin, A.C. (2013). Interactome map uncovers phosphatidylserine transport by oxysterol-binding proteins. Nature *501*, 257–261.

Moravcevic, K., Mendrola, J.M., Schmitz, K.R., Wang, Y.H., Slochower, D., Janmey, P.A., and Lemmon, M.A. (2010). Kinase associated-1 domains drive MARK/PAR1 kinases to membrane targets by binding acidic phospholipids. Cell *143*, 966–977.

Moreau, P., Bessoule, J.J., Mongrand, S., Testet, E., Vincent, P., and Cassagne, C. (1998). Lipid trafficking in plant cells. Prog. Lipid Res. *37*, 371–391.

Moser von Filseck, J., Copic, A., Delfosse, V., Vanni, S., Jackson, C.L., Bourguet, W., and Drin, G. (2015). INTRACELLULAR TRANSPORT. Phosphatidylserine transport by ORP/Osh proteins is driven by phosphatidylinositol 4-phosphate. Science *349*, 432–436.

Noack, L.C., and Jaillais, Y. (2017). Precision targeting by phosphoinoistides: how PIs direct endomembrane trafficking in plants. Curr. Opin. Plant Biol. *40*, 22–33.

Potocky, M., Pleskot, R., Pejchar, P., Vitale, N., Kost, B., and Zarsky, V. (2014). Live-cell imaging of phosphatidic acid dynamics in pollen tubes visualized by Spo20p-derived biosensor. New Phytol. *203*, 483–494.

Preuss, M.L., Schmitz, A.J., Thole, J.M., Bonner, H.K., Otegui, M.S., and Nielsen, E. (2006). A role for the RabA4b effector protein PI-4Kbeta1 in polarized expansion of root hair cells in *Arabidopsis thaliana*. J. Cell Biol. *172*, 991–998.

Ruelland, E., Cantrel, C., Gawer, M., Kader, J.C., and Zachowski, A. (2002). Activation of phospholipases C and D is an early response to a cold exposure in *Arabidopsis* suspension cells. Plant Physiol. *130*, 999–1007.

Samalova, M., Fricker, M., and Moore, I. (2006). Ratiometric fluorescence-imaging assays of plant membrane traffic using polyproteins. Traffic *7*, 1701–1723.

Schindelin, J., Arganda-Carreras, I., Frise, E., Kaynig, V., Longair, M., Pietzsch, T., Preibisch, S., Rueden, C., Saalfeld, S., Schmid, B., et al. (2012). Fiji: an open-source platform for biological-image analysis. Nat. Methods *9*, 676–682.

Simon, M.L., Platre, M.P., Assil, S., van Wijk, R., Chen, W.Y., Chory, J., Dreux, M., Munnik, T., and Jaillais, Y. (2014). A multi-colour/multi-affinity marker set to visualize phosphoinositide dynamics in *Arabidopsis*. Plant J. *77*, 322–337.

Simon, M.L., Platre, M.P., Marques-Bueno, M.M., Armengot, L., Stanislas, T., Bayle, V., Caillaud, M.C., and Jaillais, Y. (2016). A PtdIns(4)P-driven electrostatic field controls cell membrane identity and signalling in plants. Nat. Plants *2*, 16089.

Stanislas, T., Platre, M.P., Liu, M., Rambaud-Lavigne, L.E.S., Jaillais, Y., and Hamant, O. (2018). A phosphoinositide map at the shoot apical meristem in *Arabidopsis thaliana*. BMC Biol. *16*, 20.

Testerink, C., and Munnik, T. (2011). Molecular, cellular, and physiological responses to phosphatidic acid formation in plants. J. Exp. Bot. *62*, 2349–2361.

Uchida, Y., Hasegawa, J., Chinnapen, D., Inoue, T., Okazaki, S., Kato, R., Wakatsuki, S., Misaki, R., Koike, M., Uchiyama, Y., et al. (2011). Intracellular

phosphatidylserine is essential for retrograde membrane traffic through endosomes. Proc. Natl. Acad. Sci. USA *108*, 15846–15851.

Uemura, M., Joseph, R.A., and Steponkus, P.L. (1995). Cold acclimation of *Arabidopsis thaliana* (effect on plasma membrane lipid composition and freeze-induced lesions). Plant Physiol. *109*, 15–30.

Xu, P., Baldridge, R.D., Chi, R.J., Burd, C.G., and Graham, T.R. (2013). Phosphatidylserine flipping enhances membrane curvature and negative charge required for vesicular transport. J. Cell Biol. *202*, 875–886.

Yamaoka, Y., Yu, Y., Mizoi, J., Fujiki, Y., Saito, K., Nishijima, M., Lee, Y., and Nishida, I. (2011). PHOSPHATIDYLSERINE SYNTHASE1 is required for microspore development in *Arabidopsis thaliana*. Plant J. *67*, 648–661.

Yeung, T., Gilbert, G.E., Shi, J., Silvius, J., Kapus, A., and Grinstein, S. (2008). Membrane phosphatidylserine regulates surface charge and protein localization. Science *319*, 210–213.

Yeung, T., Terebiznik, M., Yu, L., Silvius, J., Abidi, W.M., Philips, M., Levine, T., Kapus, A., and Grinstein, S. (2006). Receptor activation alters inner surface potential during phagocytosis. Science *313*, 347–351.

Zhang, F., Wang, Z., Lu, M., Yonekubo, Y., Liang, X., Zhang, Y., Wu, P., Zhou, Y., Grinstein, S., Hancock, J.F., et al. (2014). Temporal production of the signaling lipid phosphatidic acid by phospholipase D2 determines the output of extracellular signal-regulated kinase signaling in cancer cells. Mol. Cell Biol. *34*, 84–95.

STAR★METHODS

KEY RESOURCES TABLE

REAGENTS and RESOURCES	SOURCE	IDENTIFIER
Bacterial and Virus Strains		
DH5a Competent Cells	ThermoFisher Scientific	Cat#18265017
Agrobacterium tumefaciens: C58 GV3101 strain	Jaillais's lab	N/A
Antibodies		
Anti-HA	www.boehringer-ingelheim.com	RRID: AB_2532070
Anti-mouse HRP-conjugated	www.gelifesciences.com	RRID: AB_772209
Chemicals, Peptides, and Recombinant Proteins		
FM4-64	ThermoFisher Scientific	T13320
Wortmannin	Sigma-Aldrich	W1628
Brefeldin A (BFA)	Sigma-Aldrich	B7651
R59022	Sigma-Aldrich	D5919
R59949	Sigma-Aldrich	D5794
Phenylarsine oxide (PAO)	Sigma-Aldrich	P3075
BSA fatty acyl free	Sigma-Aldrich	A8806
HA-$C2^{LACT}$	this study	N/A
Lyso Phosphatidylserine 18:1	Avanti Polar Lipids	858143
Lyso Phosphatidic acid 18:1	Avanti Polar Lipids	857130
Experimental Models: Organisms/Strains		
A. thaliana: Col 0	NASC	NASC# N1092
S. cerevisiae: (BY4743)	ThermoFisher Scientific	YSC1050
S. cerevisiae: Δcho1 (YSC6275-201917366)	ThermoFisher Scientific	37756
A. thaliana: pUBQ10::mCITRINE-1xPH^{FAPP1} (P5Y)	(Simon et al., 2014)	NASC# N2105607
A. thaliana: pUBQ10::mCITRINE-2xPH^{FAPP1} (P21Y)	(Simon et al., 2014)	NASC# N2105612
A. thaliana: pUBQ10::mCITRINE-P4M^{SidM}	(Simon et al., 2016)	NASC# N2107346
A. thaliana: pUBQ10::mCITRINE-1xPH^{PLC} (P14Y)	(Simon et al., 2014)	NASC# N2105609
A. thaliana: pUBQ10::mCITRINE-2xPH^{PLC} (P24Y)	(Simon et al., 2014)	NASC# N2105613
A. thaliana: pUBQ10::mCITRINE-tubbyc (P15Y)	(Simon et al., 2014)	NASC# N2105610
A. thaliana: pUBQ10::mCITRINE-$C2^{LACT}$	(Simon et al., 2016)	NASC# N2107347
A. thaliana: pUBQ10::2xmCHERRY-$C2^{LACT}$	This study	N/A
A. thaliana: PDF1::mCITRINE-$C2^{LACT}$	This study	N/A
A. thaliana: pUBQ10::mCITRINE-2xPH^{EVCT2}	This study	N/A
A. thaliana: pUBQ10::tdTOMATO -2xPH^{EVCT2}	This study	N/A
A. thaliana: pUBQ10::mCITRINE-1xPASS	This study	N/A
A. thaliana: pUBQ10::mCITRINE-1xPASS^{NESmut}	This study	N/A

(*Continued on next page*)

Continued

REAGENTS and RESOURCES	SOURCE	IDENTIFIER
A. thaliana: pUBQ10::mCITRINE-1xPASS^{L67P}	This study	N/A
A. thaliana: pUBQ10::mCITRINE-1xPASS^{K66E,K68E}	This study	N/A
A. thaliana: pUBQ10::mCITRINE-1xPASS ^{K66E,K68E,R71E,K73E}	This study	N/A
A. thaliana: pUBQ10::mCITRINE-2xPASS	This study	N/A
A. thaliana: pUBQ10::mCITRINE-KA1^{MARK1}	(Simon et al., 2016)	NASC# N2107345
A. thaliana: pUBQ10::2xmCITRINE-8K-Farn (8+)	(Simon et al., 2016)	NASC# N2107342
A. thaliana: pUBQ10::2xmCITRINE-4K4Q-Farn (4+)	(Simon et al., 2016)	NASC# N2107343
A. thaliana: pUBQ10::2xmCITRINE-2K6Q-Farn (2+)	(Simon et al., 2016)	N/A
A. thaliana: pUBQ10::2xmCITRINE-0K8Q-Farn (0+)	(Simon et al., 2016)	NASC# N2107344
A. thaliana: 35S::EGFP-Lti6b	(Cutler et al., 2000)	NASC# N84726
A. thaliana: pUBQ10::Lti6b-2xmCHERRY	(Elsayad et al., 2016)	N/A
A. thaliana: 35S::EGFP-aqPIP2a	(Cutler et al., 2000)	NASC# N84725
A. thaliana: pUBQ10::myri-2xmCITRINE	(Simon et al., 2016)	N/A
A. thaliana: W7R – mCHERRY-RABF2a	(Geldner et al., 2009)	NASC# N781672
A. thaliana: W13R – mCHERRY-VTI12	(Geldner et al., 2009)	NASC# N781675
A. thaliana: W18R – mCHERRY-Got1p	(Geldner et al., 2009)	NASC# N781676
A. thaliana: W24R – mCHERRY-RABA5d	(Geldner et al., 2009)	NASC# N781678
A. thaliana: W34R – mCHERRY-RABA1e	(Geldner et al., 2009)	NASC# N781683
A. thaliana: W25R – mCHERRY-D1	(Geldner et al., 2009)	NASC# N781679
A. thaliana: VHA-A1-mRFP1	(Dettmer et al., 2006)	N/A
A. thaliana: VHA-A3-mRFP1	(Dettmer et al., 2006)	N/A
A. thaliana: Sec-RFP	(Samalova et al., 2006)	NASC# N799370
A. thaliana: pUBQ10::+ALPS^{GCS1}-mCITRINE	This study	N/A
A. thaliana: pUBQ10::+ALPS^{K210Q}-mCITRINE	This study	N/A
A. thaliana: pss1-3	*GABI_166G10,* (Kleinboelting et al., 2012)	NASC# N415922
A. thaliana: pss1-4	*GABI_613C03,* (Kleinboelting et al., 2012)	NASC# N458779

(*Continued on next page*)

Continued

REAGENTS and RESOURCES	SOURCE	IDENTIFIER
A. thaliana: pss1-5	*GABI_217D10,* (Kleinboelting et al., 2012)	NASC# N420782
A. thaliana: pPSS1::PSS1g/pss1-3	This study	N/A
Oligonucleotides		
For primers used in genotyping, RT-PCR and cloning see Table S2, related to STAR Methods	N/A	N/A
Recombinant DNA		
Empty gateway entry vector: pDONR221	thermofisher	cat# 12536017
Empty gateway entry vector: pDONR P4P1R	thermofisher	cat# 12537023
Empty gateway entry vector: pDONR P2RP3	thermofisher	cat# 12537023
Empty gateway destination vector: pB7m34GW	(Karimi et al., 2007)	N/A
Empty gateway destination vector: pH7m34GW	(Karimi et al., 2007)	N/A
Empty gateway destination vector: pAG425GPD-EGFP-ccdb	(Alberti et al., 2007)	addgene clone #14322
Empty gateway destination vector: pTNT-HA-ccdb	(Simon et al., 2016)	N/A
Cloning vector: pWEN240	(Potocky et al., 2014)	N/A
Gateway entry vector (promoter): UBQ10prom/ pDONR P4P1R	(Jaillais et al., 2011)	NASC# N2106315
Gateway entry vector (promoter): PDF1prom/ pENTR5'	(Stanislas et al., 2018)	N/A
Gateway entry vector (fluorescent protein): mCITRINEnoSTOP/pDONR221	(Simon et al., 2014)	NASC# N2106287
Gateway entry vector (fluorescent protein): 2xmCHERRYnoSTOP/pDONR221	(Simon et al., 2014)	N/A
Gateway entry vector (fluorescent protein): tdTOMATOnoSTOP/pDONR221	This study	N/A
Gateway entry vector (lipid binding domain): 1xPASS/pDONR P2RP3	This study	N/A
Gateway entry vector (lipid binding domain): 2xPASS/pDONR P2RP3	This study	N/A
Gateway entry vector (lipid binding domain): $1xPASS^{NESmut}$/pDONR P2RP3	This study	N/A
Gateway entry vector (lipid binding domain): $1xPASS^{L67P}$/pDONR P2RP3	This study	N/A
Gateway entry vector (lipid binding domain): $1xPASS^{K66E,K68E}$/pDONR P2RP3	This study	N/A
Gateway entry vector (lipid binding domain): $1xPASS^{K66E,K68E,R71E,K73E}$ /pDONR P2RP3	This study	N/A
Gateway entry vector (lipid binding domain): $1xPH^{EVCT2}$/pDONR P2RP3	This study	N/A
Gateway entry vector (lipid binding domain): $1xPH^{EVCT2}$/pDONR 221	This study	N/A
Gateway entry vector (lipid binding domain): $2xPH^{EVCT2}$/pDONR P2RP3	This study	N/A
Gateway entry vector (lipid binding domain): $1xC2^{LACT}$/pDONR P2RP3	(Simon et al., 2016)	N/A
Gateway entry vector (lipid binding domain): $1xC2^{LACT}$/pDONR 221	(Simon et al., 2016)	N/A
Gateway entry vector (PSS1 promotor and gDNA): promPSS1-PSS1g/pDONR 221	This study	N/A

(*Continued on next page*)

Continued

REAGENTS and RESOURCES	SOURCE	IDENTIFIER
Gateway entry vector (+ALPS domain from GCS1) +ALPS^{GCS1}/pDONR 221	This study	N/A
Gateway entry vector (+ALPS domain from GCS1 mutated + motif) +ALPS^{K210Q}/pDONR 221	This study	N/A
Gateway entry vector (PI4Kbeta1) PI4Kbeta1/ pDONR P2RP3	This study	N/A
Gateway entry vector (PI4Kbeta1 ΔCter) PI4Kbeta1ΔCter/pDONR P2RP3	This study	N/A
Gateway entry vector (+ALPS^{PI4Kbeta1}) (+ALPS^{PI4Kbeta1}/ pDONR P2RP3	This study	N/A
Gateway destination vector (for N. benthamiana transformation): pUBQ10::AGD6-mCITRINE/pB7m34GW	This study	N/A
Gateway destination vector (for N. benthamiana transformation): pUBQ10::AGD6^{L216E}-mCITRINE/pB7m34GW	This study	N/A
Gateway destination vector (for N. benthamiana transformation): pUBQ10::mCITRINE-C2^{LACT}/pB7m34GW	(Simon et al., 2016)	N/A
Gateway destination vector (for plant transformation): PDF1::mCITRINE-C2^{LACT}/pB7m34GW	This study	N/A
Gateway destination vector (for plant transformation and for N. benthamiana transformation): pUBQ10::mCITRINE-2xPH^{EVCT2}/pB7m34GW	This study	N/A
Gateway destination vector (for plant transformation): pUBQ10::mCITRINE-1xPASS/pB7m34GW	This study	N/A
Gateway destination vector (for plant transformation): pUBQ10::mCITRINE-1xPASS^{NESmut}/pB7m34GW	This study	N/A
Gateway destination vector (for plant transformation): pUBQ10::mCITRINE-1xPASS^{L67P}/pB7m34GW	This study	N/A
Gateway destination vector (for plant transformation): pUBQ10::mCITRINE-1xPASS^{K66E,K68E}/pB7m34GW	This study	N/A
Gateway destination vector (for plant transformation): pUBQ10::mCITRINE-1xPASS ^{K66E,K68E,R71E,K73E}/ pB7m34GW	This study	N/A
Gateway destination vector (for plant transformation): pUBQ10::mCITRINE-2xPASS/pB7m34GW	This study	N/A
Gateway destination vector (for plant transformation): promPSS1-PSS1g/ pB7m34GW	This study	N/A
Gateway destination vector (for plant transformation): pUBQ10::+ALPS^{GCS1}-mCITRINE/pB7m34GW	This study	N/A
Gateway destination vector (for plant transformation): pUBQ10::+ALPS^{K210Q}-mCITRINE/pB7m34GW	This study	N/A
Gateway destination vector (for N. benthamiana transformation): pUBQ10::mCITRINE-PI4KBeta1 /pB7m34GW	This study	N/A
Gateway destination vector (for N. benthamiana transformation): pUBQ10::mCITRINE-PI4KBeta1ΔCter/pB7m34GW	This study	N/A
Gateway destination vector (for N. benthamiana transformation): pUBQ10::mCITRINE-+ALPS^{PI4KBeta1}/pB7m34GW	This study	N/A
Gateway destination vector (for N. benthamiana transformation): 2x35S::MAP-mTU2-SAC1 /pK7m34GW	(Simon et al., 2016)	N/A

(*Continued on next page*)

Continued

REAGENTS and RESOURCES	SOURCE	IDENTIFIER
Gateway destination vector (for N. benthamiana transformation): 2xp35S::MAP- mTURQUOISE2-SAC1^{DEAD}/pK7m34GW	(Simon et al., 2016)	N/A
Gateway destination vector (for N. benthamiana transformation): pUBQ10:mCITRINE- P4M^{SidM}/pB7m34GW	(Simon et al., 2016)	N/A
Gateway destination vector (for N. benthamiana transformation): pUBQ10:2xmCHERRY- KA1^{MARK1}/pH7m34GW	This study	N/A
Gateway destination vector (for yeast transformation): pAG425GPD-EGFP-C2^{LACT}	(Simon et al., 2016)	N/A
Gateway destination vector (for yeast transformation): pAG425GPD-EGFP-1xPH^{EVCT2}	This study	N/A
Gateway destination vector (for in vitro transcription/translation): HA-C2^{LACT}/pTNT	This study	N/A
Pollen transformation vector (for transient transformation): Lat52::YFP-C2^{LACT}/pWEN240	This study	N/A
Vector used as PCR template: Lact-C2-GFP-p416	(Yeung et al., 2006)	Addgene #22853
Vector used as PCR template: pEGFP-C1-1xPASS	(Zhang et al., 2014)	N/A
Vector used as PCR template: 2xPASS-pEGFP-C1	(Zhang et al., 2014)	N/A
Vector used as PCR template: pEGFP-C1-1xPH^{EVCT2}	(Uchida et al., 2011)	N/A
Vector used as PCR template: pRS416-ADH-Gcs1(186-285)-GFP	(Xu et al., 2013)	N/A
Vector used as PCR template: pRS416-ADH-Gcs1(186-285)K210Q-GFP	(Xu et al., 2013)	N/A
Software and Algorithms		
FIJI	(Schindelin et al., 2012)	https://fiji.sc/
RootTrace	(French et al., 2009)	http://www.plant-image-analysis.org/software/roottrace
JACoP	(Bolte and Cordelieres, 2006)	https://imagej.nih.gov/ij/plugins/track/jacop.html
SiCE SpotDetectorV3	Jaillais's lab	http://www.ens-lyon.fr/RDP/SiCE/METHODS_files/SiCE%20SpotDetectorV3.ijm
RootgrowthrateMacro	Jaillais's lab	N/A
ColocalizationMacro	Jaillais's lab	N/A
SpotdescriptorMacro	Jaillais's lab	N/A
ColocalizationmapMacro	Jaillais's lab	N/A
IntensitycolocalizationspotMacro	Jaillais's lab	N/A
Other		
Invitrogen™ SuperScript™ VILO™ cDNA Synthesis Kit	Fischer Scientific	11754-050
Spectrum™ Plant Total RNA Kit	Sigma-Aldrich	STRN250
Corning® Costar® TC-Treated Multiple Well Plates	Sigma-Aldrich	CLS3513
Gibson Assembly® Cloning Kit	NEB	E5510S

CONTACT FOR REAGENT AND RESOURCE SHARING

Further information and requests for resources and reagents should be directed to and will be fulfilled by the Lead Contact, Yvon Jaillais (yvon.jaillais@ens-lyon.fr).

EXPERIMENTAL MODEL AND SUBJECT DETAILS

Growth Condition and Plant Materials

Arabidopsis thaliana Columbia-0 (Col0) accession was used as wild type (WT) reference background throughout this study. *Arabidopsis thaliana* and *Nicotiana benthamiana* plants were grown in soil under long-day conditions at 21°C and 70% humidity and *in vitro* on Murashige and Skoog (MS) Basal Medium supplemented with 0.8% plant agar (pH 5.7) in continuous light conditions at 21°C. Tobacco (Nicotiana tabacum cv. Samsun) pollen was cultivated on the rich medium solidified with 0.25% (w/v) phytagel according to Potocky et al. (2014).

Plant Transformation and Selection

Each construct was transformed into *C58 GV3101 Agrobacterium tumefaciens* strain and selected on YEB media (5g/L beef extract; 1g/L yeast extract; 5g/L peptone; 5g/L sucrose; 15g/L bactoagar; pH 7.2) supplemented with antibiotics (Spectinomycin, Gentamycin). After two days of growth at 28°C, bacteria were collected using a single-use cell scraper, re-suspended in about 200 mL of transformation buffer (10mM MgCl2; 5% sucrose; 0.25% silweet) and plants were transformed by dipping. Plants from the Columbia–0 (Col0) accession were used for transformation.

Primary transformants (T1) were selected *in vitro* on the appropriate antibiotic/herbicide (glufosinate for mCITRINE, hygromycin for mCHERRY-tagged proteins). Approximately 20 independent T1s were selected for each line. In the T2 generation at least 3 independent transgenic lines were selected using the following criteria when possible: i) good expression level in the root for detection by confocal microscopy, ii) uniform expression pattern, iii) single insertion line (1 sensitive to 3 resistant segregation ratio) and, iv) line with no obvious abnormal developmental phenotypes. Lines were rescreened in T3 using similar criteria as in T2 with the exception that we selected homozygous lines (100% resistant). At this step, we selected one transgenic line for each marker that was used for further analyses and crosses.

For transient assay analyses, *A. tumefaciens* strain *GV3101* carrying the given construct was propagated on appropriate antibiotic selection plates and let to grow for 48 h at 28°C. Cultures were then resuspended in 5 mL MES buffer (10 mM MgCl2, 10 mM MES, 150 μM acetosyringone) and the bacterial concentration was adjusted to obtain an OD600 nm between 0.1- 0.5. *A. tumefaciens* strain *GV3101* carrying the given construct was next syringe-infiltrate in 2.5- week-old N. benthamiana plants (2 leaves per plant). Observations were conducted two days post infiltration, using spinning disk confocal microscopy.

The pollen expression vector was transferred into tobacco pollen grains germinating on solid culture medium by particle bombardment as described previously (Potocky et al., 2014). Particles were coated with 1 μg of DNA.

Yeast

Both, WT strain BY4743 Ref. YSC1050 (Thermo scientific, http://www.thermoscientific.fr/) and *cho1Δ* Ref. YSC6275-201917366 clone ID 37756 (Thermo scientific, http://www.thermoscientific.fr/) were grown at 30°C with YPD media and transformed using the Li-Ac mediated yeast transformation method described in (Gietz et al., 1995). Transformed yeasts were grown in YPD –Leu media at 30°C for 3-5 days.

METHOD DETAILS

Microscopy Setup

All imaging experiments were performed with the following spinning disk confocal microscope set up, except when indicated otherwise (see bellow): inverted Zeiss microscope (AxioObserver Z1, Carl Zeiss Group, http://www.zeiss.com/) equipped with a spinning disk module (CSU-W1-T3, Yokogawa, www.yokogawa.com) and a ProEM+ 1024B camera (Princeton Instrument, http://www.princetoninstruments.com/) using a 63x Plan- Apochromat objective (numerical aperture 1.4, oil immersion). GFP was excited with a 488 nm laser (150mW) and fluorescence emission was filtered by a 525/50 nm BrightLine® single-band bandpass filter (Semrock, http://www.semrock.com/). YFP/mCITRINE were excited with a 515 nm laser (60mW) and fluorescence emission was filtered by a 578/105 nm BrightLine® single-band bandpass filter (Semrock, http://www.semrock.com/), CHERRY/RFP were excited with a 561 nm laser (80mW) and fluorescence emission was filtered by a 609/54 nm BrightLine® single-band bandpass filter (Semrock, http://www.semrock.com/). 488 or 515 nm laser and 561 nm laser were used to excite GFP or YFP/mCITRINE and RFP/mCHERRY, respectively. For quantitative imaging, pictures of epidermal root meristem cells were taken with detector settings optimized for low background and no pixel saturation. Care was taken to use similar confocal settings when comparing fluorescence intensity or for quantification. Yeasts were visualized by spinning disk microscopy using 100X objective (Plan-apochromatic, numerical aperture 1.46) and 488nm laser.

mCITRINE-C2^{LACT} imaging of shoot tissues were performed on a Leica SP8 up-right confocal microscope (Leica, Wetzlar, Germany), with a water immersion objective (HCX IRAPO L 25x/0.95 W), and a 488 nm led laser. Fluorescence emission was detected at 525-600 nm.

Colocalization between mCITRINE-C2^{LACT} and VHA-A3-RFP, were acquired on an inverted Zeiss CLSM710 confocal microscope as previously described (Simon et al., 2014).

For pollen tube live-cell imaging, 6-9-h-old pollen tubes were observed using a spinning-disc confocal microscope (Yokogawa CSU-X1 on Nikon Ti-E platform) equipped with a 60X Plan Apochromat objective (WI; numerical aperture = 1.2) and an Andor Zyla sCMOS camera. Laser excitation at 488 nm, together with a 542/27-nm single-band filter (Semrock Brightline) were used for fluorescence collection of YFP.

Time Lapse Imaging

Time lapse imaging of cell division and root hair growth were performed as described (Doumane et al., 2017). In brief, five days old Arabidopsis seedlings were transferred in a chambered cover glass (Lab-Tek II, www.thermoscientific.com), which contained 1.5 ml of MS medium (pH 5.7) containing 0.8% plant agar (Duchefa, http://www.duchefa-biochemie.nl/) in the absence of sucrose. Epidermal cells in the meristematic region of the root (to image cytokinesis) or growing root hairs were subjected to time-lapse imaging with spinning disk confocal microscope. Two or three roots were observed simultaneously and images were collected at different Z-positions every 3 min (cytokinesis) or every 5 minutes (root hair).

Shoot Apical Meristem Imaging

To access the inflorescence meristem, flowers and floral buds were dissected out and imaged on a Leica SP8 up-right confocal microscope (Leica, Wetzlar, Germany). Fluorescence emission was detected at 525-600 nm in sequential line scanning mode with a line average of 4 and stacks of serial optical sections were generated. Projections of the signal in the L1 layer were obtained using MorphoGraphX software (http://www.mpipz.mpg.de/MorphoGraphX), according to parameter describe in MorphoGraphX User manual (http://www.mpipz.mpg.de/4085950/MGXUserManual.pdf).

FM4-64, BFA, WM, PAO, R59022, R59949 and Cold Treatments

The plasma membrane and endosomes of 5 to 7-day old transgenic lines expressing mCITRINE-C2^{LACT} were stained by incubating roots with 1 μM FM4-64 (thermofisher scientific, www.thermofisher.com) liquid MS solution for 60 min. Lines co-expressing mCITRINE-C2^{LACT} and VHA-A1-RFP were incubated in wells containing 25 μM Brefeldin A (BFA, Sigma, www.sigmaaldrich.com, BFA stock solution at 50 mM in DMSO) liquid MS solution for 60 min. Lines co-expressing mCITRINE-C2^{LACT} and W7R were incubated in wells containing 30 μM Wortmannin (Sigma, www.sigmaaldrich.com, WM stock solution at 30 mM in DMSO) liquid MS solution for 90 min. Lines co-expressing mCITRINE-C2^{LACT} with compartment markers (W25R, W13R, W18R, W7R) and 2xmCITRINE$^{8K\text{-}FARN}$ (8+) with compartment markers (W25R, W34R W7R) and 2xmCITRINE$^{4K4Q\text{-}FARN}$ (4+) with compartment markers (W25R, W13R, W18R, W7R) were incubated in wells containing 60 μM PAO (Sigma, www.sigmaaldrich.com, PAO stock solution at 60 mM in DMSO) liquid MS solution for 30 minutes. Lines expressing (Lti6b-GFP, mCITRINE-C2^{LACT}, mCITRINE-1xPH^{PLC}, mCITRINE-1xPH^{FAPP1}, mCITRINE-1xPASS, mCITRINE-2xPASS, mCITRINE-KA1^{MARK1}, 2xmCITRINE$^{8K\text{-}FARN}$ (8+)) were incubated in wells containing 12.5 μM R59022 or R59949 (Sigma, www.sigmaaldrich.com, stock solution at 25 mM in DMSO) liquid MS solution. For concomitant treatment (PAO and R599022) lines expressing (Lti6b-GFP, mCITRINE-C2^{LACT}, mCITRINE-1xPH^{PLC}, mCITRINE-1xPH^{FAPP1}, mCITRINE-1xPASS, mCITRINE-KA1^{MARK1}, 2xmCITRINE$^{8K\text{-}FARN}$ (8+)) were incubated in wells containing first liquid MS solution with PAO at 30 μM for 60 min and then were transferred into wells containing liquid MS solution with PAO at 30 μM and R59949 at 12.5 μM for 60 min. For each treatment, the mock condition corresponds to incubation of plants in well supplemented with a volume of DMSO equivalent to the highest drug concentration used and for the same time as the actual treatment. Previous to cold treatment, 12-well plate loaded with liquid MS solution was placed on ice in a cold room at 4°C for 30 minutes. Then, 5 to 7-day old transgenic lines expressing mCITRINE-1xPASS were incubated in wells placed on ice containing liquid MS solution between 4-6°C and at RT for control conditions for 1 hour. In all cases, roots were imaged within a 10-minute time frame window around the indicated time.

Dissociation Index

The effects of PAO, R59022, R59949 and PS depletion (lyso-PS add-back in the *pss1-3* and lyso-PS/lyso-PA add-back in R59949 treated plants) on the localization of our charge biosensors were analyzed by calculating the "dissociation index". First, we calculated "indexMock": the ratio between the fluorescence intensity (Mean Grey Value function of Fiji software) measured in two elliptical region of interest (ROIs) from the plasma membrane region (one at the apical/basal PM region and one in the lateral PM region) and two elliptical ROIs in the cytosol in the mock condition. "IndexMock" was quantified in 150 cells over three independent replicates (50 cells per replicate). Next, we measured a similar ratio in perturbed conditions ("indexExp"). "indexExp" was also quantified in 150 cells over three independent replicates (50 cells per replicate). The dissociation index is the ratio of (indexMock)/(indexExp). This dissociation index reveals the degree of relocalization of the fluorescent reporters from the plasma membrane to the cytosol, between the mock and perturbed conditions (pharmacological treatment or mutant).

In Figure 4F, the percentage of cell with mCITRINE-KA1^{MARK1} at the plasma membrane was counted by eye, by counting the number of cell with visible plasma membrane labeling and the total number of cells in each condition. Triplicate experiments were performed and at least 15 independent roots were analyzed.

Subcellular and Phenotype Complementation with Lysophospholipids

For complementation of the subcellular localization of PA sensor, 5 to 7-day old transgenic lines expressing mCITRINE-1xPASS were concomitantly treated with R59949 and lysophosphatidic acid (lyso-PA, 54μM) or lysophosphatidylserine (lyso-PS, 54μM) for 60 min in 12-well plates. For complementation of the subcellular localization of PS sensors, 8 to 12-day old transgenic lines expressing mCITRINE-C2^{LACT} or mCITRINE-2xPH^{EVCT2} in *pss1-3* were treated with lyso-PA or lyso-PS at 54μM for 60 min in 12-well plates. For complementation of the root growth rate, plants grown for 8 days on MS plates were transferred to plate containing control media (BSA only) or media supplemented with BSA + lyso-PS at 2.47μM for 3 days (lyso-PS:BSA molar ratio 4:1). Root size was quantified each day following the procedure described below. For complementation of the rosette size, plants were grown for 8 days on MS plates, transferred on control media (BSA only) or lyso-PS media (see above) for 6 days, and then transferred to soil for 8 days. Finally, plants were imaged and rosette size was quantified (see bellow). 3-5 day old yeasts expressing mCITRINE-C2^{LACT} were treated with lyso-PS with BSA (4:1) at 54μM for 60 min in 12-well plates.

Colocalization Analyses

For quantitative co-localisation, we used an object-based analysis method (OBA). OBA is used to determine the centroid of each spot (intracellular compartment) and to compare their respective localization. Co-localization between the two structures is validated if the distance between the two centroids is below the optical resolution (Bolte and Cordelieres, 2006). The OBA was performed as followed; first the intracellular compartments were automatically detected in each channel applying a ''DoG'' filter with a sigma of 3, and then a ''Triangle'' thresholding was applied (Bayle et al., 2017). Next, with the binary images obtained we used JACoP plugin on Fiji (Bolte and Cordelieres, 2006) to acquire quantitative data of the co-localization with the following parameters: minimum size of 3 μm^2 and maximum size of 20 μm^2. To allow high throughput data processing, this analysis pipeline has been automatized on a Fiji macro.

The percentage of colocalization always corresponds to the proportion of spots in the yellow channel that colocalize with spots in the red channel, except when 2xmCHERRY-C2^{LACT} was used (Figure 5F), in which case the percentage of colocalization corresponds to the proportion of spots in the red channel (2xmCHERRY-C2^{LACT}) that colocalize with spots in the yellow channel (membrane charge reporters mCITRINE$^{4K4Q\text{-}FARN}$ (4+), mCITRINE$^{2K6Q\text{-}FARN}$ (2+), 2xmCITRINE$^{8Q\text{-}FARN}$ (0+)). In other words, the percentage of colocalization corresponds to the number of spot detected in the yellow channel (mCITRINE-C2^{LACT}, mCITRINE-PH^{EVCT2}, mCITRINE$^{8K\text{-}FARN}$ (8+), mCITRINE$^{4K4Q\text{-}FARN}$ (4+), mCITRINE$^{2K6Q\text{-}FARN}$ (2+), 2xmCITRINE$^{8Q\text{-}FARN}$ (0+)), colocalizing with spots detected in the red channel (compartment markers) divided by the total number of spots detected in the yellow channel and multiplied by hundred. In order to avoid artefacts due to low number of spots detected in one of the channels, a ratio was applied. This ratio corresponds to the number of spots detected in ''Image A'' divided by the number of spots detected in ''Image B''. If the ratio was either above 2 or below 0.5 the corresponding results were discarded. This rule was not applied for colocalization with 2xmCITRINE$^{8K\text{-}FARN}$ (8+) that is massively localized at the PM and seldom in intracellular compartments (justifying a low number of spots detected in yellow channel). Co-localization was quantified in at least 8 independent roots for untreated conditions in duplicates (Figure 5). For treated conditions (Figure 6), triplicate experiments were performed and at least 15 independent roots were analyzed for quantification in mock conditions and treated conditions. To estimate the approximate number of cell present in one image, we counted the number of cells in 14 independent roots. We found an average of 43 cells per root image (meristematic/elongation zone of root epidermal cells). This allowed us to estimate the number of cells that were used for each colocalization analysis (Figures 5 and 6).

Quantification of Normalized Fluorescence Intensity in Colocalizing Spots

Binary images representing colocalizing spots (in white) between image A and image B (image A, mCTRINE-C2^{LACT} and mCITRINE-4+ and image B, red compartment makers) were obtained using JACoP as shown in Figure S5F. Colocalizing spots were selected and reported on image A (mCITRINE-C2^{LACT} or mCITRINE-4+) to quantify the average integrated density in colocalizing spots. The average integrated density in colocalizing spot was divided by the average integrated density of the global image in order to normalize the quantification. The normalized integrated density was compared between each sample. All this process was automatized using two macros on Fiji, ColocalizationmapMacro and IntensitycolocalizationspotMacro.

ALPS Motif Detection and Representation

Detection and representation of ALPS motif were performed using HELIQUEST software on the following website (http://heliquest.ipmc.cnrs.fr/, Gautier et al., 2008).

Genotyping and Characterization of *pss1* T-DNA Insertion Lines

Characterization of pss1 *T-DNA Insertions*

pss1-3 (GABI_166G10), *pss1-4* (GABI_613C03), *pss1-5* (GABI_217D10) were produced by the GABI-KAT consortium (Kleinboelting et al., 2012) and provided by the NASC (http://arabidopsis.info/BasicForm). genomic DNA was extracted from wild type, *pss1-3,*

pss1-4, pss1-5 plants using Edwards buffer and PCR and border sequencing were performed with primers starting by "Geno" in Table S2 (related to STAR Methods).

PSS1 *Transcript Expression by RT-PCR*

total mRNA was extracted from wild type, *pss1-1, pss1-3, pss1-4* and *pss1-5* using Sigma-Aldrich Spectrum™ Plant Total RNA Kit and cDNA was produced using Invitrogen, SuperScript™ VILO™ cDNA Synthesis Kit. The expression of *PSS1* and the ubiquitous *TCTP* transcripts was tested by PCR using primers starting with "RT" in Table S2.

pss1 *Segregation Analyses*

In order to analyze the segregation of *pss1-3, pss1-4, pss1-5* T-DNA lines; seeds from self-fertilized *pss1-3, pss1-4, pss1-5* heterozygous plants were grown on plate containing the antibiotic sulfadiazine. Wild type plants (sulfadiazine sensitive plants) were counted after 12 days and resistant plants (heterozygous and homozygous) were transferred to soil. 20 days later, homozygous and heterozygous *pss1* plants were identified based on their rosette phenotype and counted.

Quantification of the Root Length and Root Growth Rate

The root length was determined on stratified 12-day-old vertically grown seedlings and measured by hands using FIJI software. For the root growth rate, plants were transferred in plates supplemented with BSA only or BSA+lyso-PS and scanned each day with an EPSON scanner perfection V300 PHOTO at 800 dpi for the next three days. Images scanned at different time points were stacked using "Images to stack" function of the Fiji software with the "Copy (Center)" method and analyzed using RootTrace (French et al., 2009). To allow high throughput data analyses, the process has been automatized on a Fiji macro. The starting point for quantification corresponds to the size of the root when the plants were transferred into media supplemented with lyso-PS. The corresponding root growth rate represents the growth of the root for each day in millimeters.

Quantification of the Rosette Area

8 days after transferring plants into soil, rosettes were imaged using a CANON EOS 450D with a SIGMA DC 18-50 mm 1:2.8 EX MACRO lens at 278 pixels/cm. Fiji was used to apply an auto threshold "Percentile white" on images to obtain white rosette on black background. Then, the "wand (tracing) tool" on Fiji was used to identify the rosette rims, allowing measurement of the rosette area with Fiji measure tools (Ctrl+M).

Cloning

Preparation of Gateway Compatible Entry Clones (Entry Vector)

Published are listed in the recombinant DNA table.

PA Biosensors

The *1xPASS* and *2xPASS* sequences were amplified from *pEGFP-C1-1xPASS* and *2xPASS-pEGFP-C1* plasmids (gift from Gangwei Du) (Bohdanowicz et al., 2013; Zhang et al., 2014). Gateway compatible PCR products were introduced into *pDONRP2R-P3* vectors by BP recombination using the following primers: *PASS-P2RP3_R* and *PASS-P2RP3wSTOP_R* to give *1xPASS/pDONR P2RP3* and *PASS-P2RP3_R* and *2xPASS-B3wstop_R* to give *2xPASS/pDONR P2RP3*.

Mutations in PASS were obtained by successive site directed mutagenesis using the following partially overlapping forward (FP) and reverse (RP) primers:

NESmut_F and NESmut_R using 1xPASS/pDONRP2RP3 as template to give $1xPASS^{NESmut}$/pDONR P2RP3

PASSmut(L67P)_F and PASSmut(L67P)_R using 1xPASS/pDONRP2RP3 as template to give $1xPASS^{(L67P)}$/pDONR P2RP3

PASSmut(K66E&K68E)_F and PASSmut(K66E&K68E)_R using 1xPASS/pDONRP2RP3 as template to give $1xPASS^{(K66E,K68E)}$/pDONR P2RP3

PASSmut(K71E&K73E)_F and PASSmut(K71E&K73E)_R using $1xPASS^{(K66E,K68E)}$/pDONRP2RP3 as template to give $1xPASS^{(K66E,K68E,K71E,K73E)}$/pDONR P2RP3

PS Biosensors

The PH^{EVCT2} sequence was amplified from *pEGFP-C1-1xPH*^{EVCT2} plasmid (gift from Tomohiko Taguchi) (Uchida et al., 2011). Gateway compatible PCR products were introduced into *pDONRP2R-P3* or *pDONR221* vectors by BP recombination using the following primers: *EVECTIN2-P2RP3_F* and *EVECTIN2-P2RP3_R* or *1xPH-EVCT2-p221wSTOP_F* and *1xPH-EVCT2-p221wSTOP_R* to give *1xPH*^{EVCT2}*/pDONRP2RP3* or *1xPH*^{EVCT2}*/pDONR221*, respectively.

To produce *2xPH*^{EVCT2}*/pDONRP2RP3*, the *1xPH*^{EVCT2}*/pDONR P2RP3* plasmid was amplified using *BackBone_1xPH-EVECT_F* and *BackBone_1xPH-EVECT_R* primers and *1xPH*^{EVCT2} was amplified using *INSERT-PH-EVECT2_F* and *INSERT-PH-EVECT2_F* primers. Both PCR products were assembled by Gibson cloning (New England biolabs, https://www.neb.com/) to give *2xPH*^{EVCT2}*/pDONRP2RP3*.

For the cloning of *Lat52:YFP-C2*^{LACT}*, C2*^{LACT} sequence flanked by NgoMIV/ApaI sites was amplified from *Lact-C2-GFP-p416* plasmid (Addgene #22853) by PCR using specific primers *Lact-C2_F* and *Lact-C2_R*. Amplified products were introduced into the multiple cloning sites of pollen expression vectors *pWEN240* using NgoMIV/ApaI restriction enzyme sites. The *pWEN240* vector (Potocky et al., 2014) was kindly provided by Prof. Benedikt Kost (University of Erlangen-Nuremberg, Erlangen, Germany).

PSS1 *Genomic Sequence*

PSS1 (*At1g15110*) genomic sequence was amplified from genomic DNA extracted from *Arabidopsis thaliana* wild type plants (Col0 ecotype) using Edwards buffer. The entire genomic fragment (*promoter+gene*) was amplified using gateway compatible

primers *promPSS1-p221*_F and *gPSS1-p221_R*, and the corresponding PCR product was introduced into the *pDONR221* vector by BP recombination to give *promPSS1::PSS1g/pDONR221.*

+ALPS Sensor

The *+ALPS*^{GCS1} and *+ALPS*^{K210Q} sequence were amplified from *pRS416-ADH-Gcs1(186-285)-GFP* and *pRS416-ADH-Gcs1(186-285)K210Q-GFP* plasmids, respectively (Xu et al., 2013), using the following primers: *+ALPS*^{GCS1}*_F* and *+ALPS*^{GCS1}*_R*. Gateway compatible PCR products were introduced into pDONR221 vector by BP recombination to give *+ALPS*^{GCS1}*/pDONR221* and *+ALPS*^{K210Q}*/pDONR221*.

PI4Kβ1

PI4Kβ1 (At5g64070), PI4Kβ1ΔCter and *+ALPS*$^{PI4K\beta1}$ were amplified by PCR from Col0 cDNA, using the following primers, *PI4Kbeta1_F* and *PI4Kbeta1_R* or *PI4Kbeta1_F* and *PI4Kbeta1-no+ALPS_R* or *+ALPS*^{PI4Kbeta1}*_F* and *+ALPS*^{PI4Kbeta1}*_R,* respectively. Gateway compatible PCR products were introduced into *pDONR P2RP3*, to give, *PI4Kβ1/pDONR P2RP3*, *PI4Kβ1ΔCter/pDONR P2RP3* and *+ALPS*$^{PI4K\beta1}$*/pDONR P2RP3*, respectively.

AGD6

AGD6 (*At3g53710*) was amplified by PCR from Col0 cDNA using the following primers, *AGD6_F* and *AGD6_R*. Gateway compatible PCR products were introduced into *pDONR221* to give*, AGD6/pDON221. AGD6*^{L216E} was obtained by site directed mutagenesis using the following primers *L216E_F* and *L216E_R.*

Construction of Destination Clones (Destination Vector)

Published destination vectors are listed in the recombinant DNA table (Key Resource Table).

Binary destination vectors for plant transformation were obtained using the multisite LR recombination system (life technologies, http://www.thermofisher.com/) using the pB7m34GW (basta resistant) and pH7m34GW (hygromycin resistant) (Karimi et al., 2007) as destination vectors. All mCITRINE-containing clones are in *pB7m34GW* and all mCHERRY-containing clones are in *pH7m34GW* to produce the following destination vectors: *pPSS1::PSS1g/pB7m34GW, pUBQ10::mCITRINE-2xPASS/pB7m34GW, pUBQ10::2xmCHERRY-C2*^{LACT}*/pH7m34GW, PDF1::mCITRINE-C2*^{LACT}*/pB7m34GW, pUBQ10::mCITRINE-2xPH*^{EVCT2}*/pB7m34GW, pUBQ10::tdTOMATO-2xPH*^{EVCT2}*/pH7m34GW, pUBQ10::mCITRINE-1xPASS/pB7m34GW, pUBQ10::mCITRINE-1xPASS*^{NESmut}*/pB7m34GW, pUBQ10::mCITRINE-1xPASS*^{L67P}*/pB7m34GW, pUBQ10::mCITRINE-1xPASS*^{K66E,K68E}*/pB7m34GW, pUBQ10::mCITRINE-1xPASS*^{K66E,K68E,R71E,K73E}*/pB7m34GW, pUBQ10::+ALPS*^{GCS1}*-mCITRINE/pB7m34GW and pUBQ10::+ALPS*^{K210Q}*-mCITRINE/pB7m34GW, pUBQ10:: mCITRINE-PI4KBeta1/pB7m34GW, pUBQ10::mCITRINE-PI4KBeta1ΔCter/pB7m34GW, pUBQ10::mCITRINE+ALPS*^{PI4KBeta1}*/pB7m34GW, pUBQ10::AGD6-mCITRINE/pB7m34GW, and pUBQ10::AGD6*^{L216E}*-mCITRINE/pB7m34GW. 1xPH*^{EVCT2} was recombined with *pAG425GPD-EGFP-ccdb* (addgene clone #14322, gift of Susan Lindquist, (Alberti et al., 2007)) destination vector for N-terminal GFP tagging.

In vitro Assay

Recombinant Protein Expression and Lipid-Protein Overlay Assays

The expression plasmid (*pTNT::HA-C2*^{LACT}) was used as DNA template for *in vitro* transcription and translation using the TNT® SP6 High-Yield Wheat Germ Protein Expression System (Promega, www.promega.com), following manufacturer's instructions. 5μl of the total reaction were used to analyze protein expression levels by western-blot using 1:1000 anti-HA (www.boehringer-ingelheim.com) primary antibodies and 1:5000 secondary anti-mouse (GE Healthcare Life Sciences, http://www.gelifesciences.com/) antibody. The lipid overlay assays were performed as follow: nitrocellulose membranes containing immobilized purified lipids (PIPstrip P-6001, Echelon Bioscience, http://echelon-inc.com/) were incubated for 1h in blocking solution (TBST (50 mM Tris, 150 mM NaCl, 0,05% Tween 20, pH 7.6) + 3% BSA). Membranes were then incubated for 2h with 10 mL of blocking solution containing 40 μl of *in vitro* synthesized proteins. After three washing steps using blocking solution, membranes were incubated for 2h at room temperature with primary antibodies diluted in blocking solution, rinsed three times with blocking solution and incubated for 1h at room temperature with the secondary antibody also diluted in blocking solution. Antibodies and dilutions are the same as described above.

Lipid Quantification for Lipid Measurement in *pss1* Mutant (HPTLC and LC-MS/MS)

Lipid Extraction

Leaves of 28-day old plants (0.1-1g fresh weight) were collected in glass tubes; 2 ml of preheated isopropanol were added and tubes were heated at 70°C for 20 min to inhibit phospholipase D activity. 6 ml of chloroform/methanol 2/1 (v/v) were added and lipid extraction was completed at room temperature. The organic phases were transferred to new glass tubes. Then 1.5 ml of H_2O was added to the organic phases and tubes were vortexed and centrifuged at 2000 rpm; the organic phases were transferred to new glass tubes, evaporated and the lipids were resuspended in the appropriate volume of chloroform/methanol 2/1, v/v, in order to obtain the same concentration according to the initial seedlings fresh weight.

High Performance Thin-layer Chromatography (HPTLC)

Lipids were deposited on HPTLC plates (Silica gel 60G F_{254} glass plates Merck Millipore) together with external pure lipid standards (Avanti lipids). Plates were developed according to (Heape et al., 1985). Following chromatography, the lipids were charred for densitometry according to (Macala et al., 1983)). Briefly, plates were dipped into a 3% cupric acetate (w/v)-8% orthophosphoric acid (v/v) solution in H_2O and heated at 110°C for 30 min. Plates were scanned at 366 nm using a CAMAG TLC scanner 3. 8 independent samples were quantified for pss1-3 and pss1-4 and 6 samples for col0.

LC-MS/MS

For the analysis of phospholipids by LC-MS/MS, phospholipid extracts were dissolved in 100 μL of eluent A (isopropanol/methanol/water 5/1/4 + 0.2% formic acid + 0.028% NH_3) containing synthetic internal lipid standards (PS 17:0/17:0; PE 17:0/17:0; PI 17:0/14:1 and PC 17:0/14:1 from Avanti Polar Lipids). LC-MS/MS (multiple reaction monitoring mode) analyses were performed with a model QTRAP 5500 (ABSciex) mass spectrometer coupled to a liquid chromatography system (Ultimate 3000; Dionex). Analyses were performed in the negative (PS, PE, PI) and positive (PC) modes with fast polarity switching (50 ms); nitrogen was used for the curtain gas (set to 15), gas 1 (set to 20), and gas 2 (set to 0). Needle voltage was at -4500 or +5500 V without needle heating; the declustering potential was adjusted between -160 and -85 V or set at +40 V. The collision gas was also nitrogen; collision energy varied from -48 to -62 eV and +47 eV on a compound-dependent basis. Reverse-phase separations were performed at 50°C on a Luna C8 150x1 mm column with 100-Å pore size and 5-μm particles (Phenomenex). The gradient elution program was as follows: 0min, 30%B (isopropanol + 0.2%formic acid + 0.028%NH_3); 5 min, 50% B; 30 min, 80% B; 31 to 41 min, 95% B. The flow rate was set at 40 mL/min, and 3 mL sample volumes were injected. The areas of LC peaks were determined using MultiQuant software (version 2.1; ABSciex) for relative phospholipid quantification. Quantification of molecular phospholipids species were performed on five independent samples for *pss1-3* and *pss1-4* and ten independent samples for Col0.

Lipid Quantification for R59949 and R59022 Treatment (HPTLC)

Treatments R59949 and R59022

8 day old seedlings (0.1-1g) were incubated in wells containing 12.5 μM R59022 or R59949 (Sigma, www.sigmaaldrich.com, stock solution at 25 mM in DMSO) in liquid MS solution for 1 hour.

Lipid Extraction

Seedling were collected in glass tubes; two ml of preheated (70°C) isopropanol were added and material was grinded. Tubes were heated at 70°C for 20 min. Two ml chloroform/methanol/HCL (100/50/1, v/v) were added at room temperature and tubes were incubated for at least one hour at room temperature. After centrifugation (500g) for 5 min, the organic phase was recovered and transferred to new glass tubes. Four ml chloroform/methanol/HCl (100/50/1, v/v) were added to the seedlings, the tubes were vortexed, then 1ml of H2O was added and tubes were vortexed again and centrifuged at 500g for 5 min. The organic phase was recovered and pooled with the previous one. Then 2 ml of NaCl 0.09% were added to the organic phase, tubes were vortexed and centrifuged at 500g for 5 min. The organic phase was recovered, evaporated, and the lipids were resuspended in the appropriate volume of chloroform/methanol (2/1, v/v) in order to obtain the same concentration according to the initial seedlings fresh weight.

Phospholipid Analysis

Phospholipids were analyzed by loading total lipids onto HPTLC plates (60F254, Merck, Darmstadt, Germany), which were developed either in methyl acetate/n-propanol/chloroform/methanol/0.25% aqueous KCl (25/25/25/10/9, v/v) or in chloroform/methanol/acetic acid/H20 (20/4.5/2/1, v/v). Lipids were identified by co-migration with known standards and quantified by densitometry analysis using a TLC scanner 3 (CAMAG, Switzerland) as described in (Kriechbaumer et al., 2018; Laloi et al., 2007). Both methods gave similar phospholipid quantifications, validating the robustness of our analyses.

QUANTIFICATION AND STATISTICAL ANALYSIS

Quantitative co-localization results were statistically compared using the Kruskal-Wallis bilateral test (p-value=0.05) using XLstat software (http://www.xlstat.com/). Pairwise comparisons between groups were performed according to Steel-Dwass-Critchlow-Fligner procedure (different letters indicate statistical difference between samples). For quantitative co-localization results of Figure 5E we used the bilateral test Kruskal-Wallis test (p-value=0.15) using XLstat software (http://www.xlstat.com/). Pairwise comparisons between groups was performed according to Dunn procedure (different letters indicate statistical difference between samples). Statistical analyses between two samples were performed using the non-parametric Wilcoxon-Mann-Whitney test (p-value=0.05).